

Energetic galaxy-wide outflows in high-redshift ultra-luminous infrared galaxies hosting AGN activity

C. M. Harrison,^{1*} D. M. Alexander,¹ A. M. Swinbank,² Ian Smail,² S. Alaghband-Zadeh,³ F. E. Bauer,^{4,5} S. C. Chapman,³ A. Del Moro,¹ R. C. Hickox,^{6,1} R. J. Ivison,^{7,8} Karín Menéndez-Delmestre,^{9,10} J. R. Mullaney¹¹ and N. P. H. Nesvadba¹²

¹Department of Physics, Durham University, South Road, Durham, DH1 3LE, UK

²Institute for Computational Cosmology, Durham University, South Road, Durham, DH1 3LE, UK

³Institute of Astronomy, Madingley Road, Cambridge, CB3 0HA, UK

⁴Space Science Institute, 4750 Walnut Street, Suite 205, Boulder, CO 80301, USA

⁵Pontificia Universidad Católica de Chile, Departamento de Astronomía y Astrofísica, Casilla 306, Santiago 22, Chile

⁶Department of Physics and Astronomy, Dartmouth College, 6127 Wilder Laboratory, Hanover, NH 03755, USA

⁷UK Astronomy Technology Centre, Royal Observatory, Blackford Hill, Edinburgh, EH9 3HJ, UK

⁸Institute for Astronomy, University of Edinburgh, Blackford Hill, Edinburgh, EH9 3HJ, UK

⁹Observatório do Valongo, Universidade Federal do Rio de Janeiro, Ladeira Pedro Antônio, 43, Saúder CEP 20080-090 Rio de Janeiro, RJ, Brazil

¹⁰California Institute of Technology, MC 249-17, Pasadena, CA 91125, USA

¹¹Laboratoire AIM-Paris-Saclay, CEA/DSM/Irfu - CNRS, Université Paris Diderot, CE-Saclay, pt courrier 121, 91191 Gif-sur-Yvette, France

¹²Institut d'Astrophysique Spatiale, Université Paris-Sud, Bat. 120-121, 91405 Orsay, France

*Email: c.m.harrison@durham.ac.uk

12 June 2018

ABSTRACT

We present integral field spectroscopy observations, covering the [O III] $\lambda\lambda$ 4959,5007 emission-line doublet of eight high-redshift ($z=1.4\text{--}3.4$) ultra-luminous infrared galaxies (ULIRGs) that host Active Galactic Nuclei (AGN) activity, including known sub-millimetre luminous galaxies (SMGs). The targets have moderate radio luminosities that are typical of high-redshift ULIRGs ($L_{1.4\text{GHz}}=10^{24}\text{--}10^{25}\text{ W Hz}^{-1}$) and therefore are not radio-loud AGN. We de-couple kinematic components due to the galaxy dynamics and mergers from those due to outflows. We find evidence in the four most luminous systems ($L_{[\text{O III}]}\gtrsim 10^{43}\text{ erg s}^{-1}$) for the signatures of large-scale energetic outflows: extremely broad [O III] emission (FWHM $\approx 700\text{--}1400\text{ km s}^{-1}$) across $\approx 4\text{--}15\text{ kpc}$, with high velocity offsets from the systemic redshifts (up to $\approx 850\text{ km s}^{-1}$). The four less luminous systems have lower quality data displaying weaker evidence for spatially extended outflows. We estimate that these outflows are potentially depositing energy into their host galaxies at considerable rates ($\dot{E}\approx 10^{43}\text{--}10^{45}\text{ erg s}^{-1}$); however, due to the lack of constraints on the density of the outflowing material and the structure of the outflow, these estimates should be taken as illustrative only. Based on the measured maximum velocities ($v_{\text{max}}\approx 400\text{--}1400\text{ km s}^{-1}$) the outflows observed are likely to unbind some fraction of the gas from their host galaxies, but are unlikely to completely remove gas from the galaxy haloes. By using a combination of energetic arguments and a comparison to ULIRGs without clear evidence for AGN activity, we show that the AGN activity could be the dominant power source for driving all of the observed outflows, although star formation may also play a significant role in some of the sources.

Key words: galaxies: high-redshift, submillimetre; — galaxies: evolution; — galaxies: star formation rates, AGN; — galaxies: individual

1 INTRODUCTION

Many of the most successful models of galaxy formation require energetic outflows over galaxy scales (i.e. $\approx 1\text{--}10\text{ kpc}$) to reproduce properties of local massive galaxies (e.g., black-hole-spheroid

mass relationship; the bright-end of the galaxy luminosity function; e.g., Silk & Rees 1998; Springel et al. 2005; Di Matteo et al. 2005; Hopkins et al. 2006, 2008; Debuhr et al. 2012). Observations show that galaxy-wide outflows can be powered by star formation and/or active galactic nuclei (AGN) activity (e.g., Heckman et al. 1990;

Crenshaw et al. 2003; Rupke et al. 2005a,b); however, most models predict that AGN-driven outflows are required in the most massive galaxies. These simulated outflows inhibit further black-hole accretion and star formation by injecting considerable kinetic energy into the interstellar medium (ISM) of the host galaxies. While theoretically attractive, these models can only be judged to be successful if supported by observational data.

AGN-driven outflows are initially launched from the accretion disk or dusty torus surrounding the black hole (BH), either in the form of a radio jet/lobe or a radiatively-driven wind. Radio jets/lobes are thought to be most effective at *heating* gas in radio-loud systems through the so-called *radio mode* (Croton et al. 2006; Bower et al. 2006) and evidence of this is observed in low-redshift massive galaxies, where mechanical heating appears to be preventing gas from cooling (e.g., Best et al. 2005, 2006; Smolčić et al. 2009; Danielson et al. 2012). In contrast, many models implement the more rapid *quasar mode*, where the radiation field produced by AGN launches a high-velocity wind which sweeps up gas in the ISM and results in a kpc-scale “outflow” (e.g., Springel et al. 2005; King 2005; Di Matteo et al. 2005; Hopkins et al. 2006; Debuhr et al. 2012). These radiatively-driven outflows are predicted to be most prevalent at high redshift, ($z \approx 2$), in luminous AGN with high accretion rates (e.g., Di Matteo et al. 2005; King 2005).

Observationally, AGN-driven winds are known to be prevalent in luminous AGN at low and high redshift: X-ray and UV absorption-line spectroscopy reveal high-velocity winds of up to $v \approx 0.1c$ (e.g., Reeves et al. 2003; Blustin et al. 2003; Trump et al. 2006; Gibson et al. 2009; Gofford et al. 2011; Page et al. 2011) and may be a ubiquitous property of all AGN (Ganguly & Brotherton 2008). However, these high-velocity winds are most likely to be produced close to the accretion disk (< 1 pc scale; e.g., Crenshaw et al. 2003; Tombesi et al. 2012). For these winds to have a global effect on the host galaxy, they must couple to the ISM and drive the gas over galaxy-wide (≈ 1 – 10 kpc) scales. To test the impact of AGN-driven outflows on the formation and evolution of galaxies, it is therefore necessary to search for kpc-scale energetic outflows.

Spatially resolved spectroscopy provides a particularly direct method to search for and characterise kpc-scale outflows. Such observations of low-redshift galaxies have identified kpc-scale outflows in both ionised (e.g., Holt et al. 2008; Fu & Stockton 2009; Rupke & Veilleux 2011; Westmoquette et al. 2012) and molecular gas (e.g., Feruglio et al. 2010; Alatalo et al. 2011). At high redshift, where accretion-related outflows are predicted to be most prevalent, integral-field unit (IFU) observations of high-redshift radio galaxies (HzRGs, at $z \approx 2$ – 3 ; Nesvadba et al. 2006, 2008) have showed that kpc-scale energetic outflows are present in at least a fraction of the high-redshift galaxy population. AGN-driven outflows were revealed in these systems through the presence of broad ($\text{FWHM} > 1000 \text{ km s}^{-1}$), high-velocity ($> 300 \text{ km s}^{-1}$) and spatially extended [O III] emission.¹ With implied velocities of greater than a few hundred km s^{-1} these outflows could potentially drive gas out of the host galaxy, inhibiting future BH growth and star formation. Recent IFU observations of the [O III], H α and

[C II] emission lines in high-redshift quasars also reveal similar outflow signatures (Cano-Díaz et al. 2012; Maiolino et al. 2012). Due to the small number of sources and the biased selection of the high-redshift galaxies studied with IFUs so far, the prevalence and significance of such galaxy-wide outflows remains poorly constrained.

Potentially the best place to search for AGN-driven outflows are high-redshift far-IR (FIR) luminous galaxies with $L_{\text{FIR}} > 10^{12} L_{\odot}$ (Ultra-Luminous Infra-Red Galaxies - ULIRGs), such as sub-millimetre galaxies (SMGs). These systems are the most intensely star-forming galaxies known with star formation rates (SFRs) of $\gtrsim 100$ – $1000 M_{\odot} \text{ yr}^{-1}$ and are thought to represent a rapid star-forming phase that every massive galaxy goes through (e.g., Swinbank et al. 2006; Tacconi et al. 2008). They have a peak space density at $z \approx 2$ – 2.5 (Chapman et al. 2004, 2005; Wardlow et al. 2011) which roughly coincides with the peak epoch of BH growth (e.g., Cattaneo & Bernardi 2003; Hopkins et al. 2007; Silverman et al. 2008). Using optical, mid-infrared and X-ray diagnostics, high-redshift ULIRGs are found to have emission dominated by starburst activity with $\approx 30\%$ of SMGs also revealing significant AGN activity (e.g., Alexander et al. 2003, 2005, 2008; Chapman et al. 2005; Ivison et al. 2010; Rafferty et al. 2011). Indeed, clustering analysis of SMGs and quasars supports the idea that starburst and AGN activity occur in the same systems (Hickox et al. 2012) and that SMGs may evolve into massive elliptical galaxies by the present day. Therefore, high-redshift ULIRGs that host AGN activity could be in transition from a star-formation dominated to an AGN dominated phase. This transition phase, which is potentially facilitated by kpc-scale outflows, is an evolutionary period required by many models (e.g., Sanders et al. 1988; Silk & Rees 1998; Springel et al. 2005; Di Matteo et al. 2005; Hopkins et al. 2006, 2008; see Alexander & Hickox 2011 for a review).

In this paper we present Gemini-North Near-Infrared Integral Field Spectrometer (NIFS) and VLT Spectrograph for Integral Field Observations in the Near Infrared (SINFONI) IFU observations of $z \approx 2$ ULIRGs with known optical AGN activity. These sources have moderate radio luminosities ($L_{1.4\text{GHz}} = 10^{24}$ – $10^{25} \text{ W Hz}^{-1}$) and can therefore be considered to be radio-quiet AGN. In §2 we give details of the IFU observations and data reduction, in §4 we present the analysis and results, in §5 we discuss the results and their implications for galaxy evolution models and in §6 we give our conclusions. We provide background information and detailed results on individual sources in Appendix A. We have adopted $H_0 = 71 \text{ km s}^{-1}$, $\Omega_M = 0.27$ and $\Omega_{\Lambda} = 0.73$ throughout; in this cosmology, $1''$ corresponds to 8.5 kpc at $z = 2.0$.

2 OBSERVATIONS AND DATA REDUCTION

2.1 Target selection

For this study we selected ten radio-detected $z = 1.4$ – 3.4 star-forming galaxies that host AGN activity to study their spatially resolved dynamics. The sample consists of eight SMGs (labelled ‘SMM’ with $850 \mu\text{m}$ flux densities $S_{850} > 4 \text{ mJy}$) and two sources that are undetected at $850 \mu\text{m}$ (labelled ‘RG’). We will collectively refer to the sample as high-redshift ULIRGs throughout. We detected [O III] emission in eight of the sources (see §4 for details). All our detected sources are [O III] luminous ($L_{[\text{O III}]} = 10^{42}$ – $10^{44} \text{ erg s}^{-1}$), and have high [N II]/H α and [O III]/H β emission-line ratios, or an AGN-dominated continuum, indicating the presence of

¹ Emission from [O III] cannot be produced in high density environments, such as the broad-line region (BLR) of AGN, without being collisionally de-excited (e.g., Osterbrock 1989; Robson 1996). Luminous ($L > 10^{42} \text{ erg s}^{-1}$), broad ($\text{FWHM} \gtrsim 1000 \text{ km}^{-1}$), and extended (\approx a few kiloparsecs) [O III] emission is therefore not associated with the BLR.

GEMINI-NORTH NIFS AND VLT SINFONI OBSERVATIONS

ID	Source	R. A.	Dec	$z_{[\text{O III}]}$	$S_{1.4}$	$L_{1.4\text{GHz}}$	AGN	t_{exp}	Average seeing	Instrument	Quality	
(1)	(2)	(J2000)	(J2000)	(5)	(μJy)	($10^{24} \text{ W Hz}^{-1}$)	(8)	(ks)	($''$)	(kpc)	(12)	(13)
1	SMMJ0217–0503	02:17:38.68	–05:03:39.5	2.021	207 ± 16	5.0	O	4.8	0.47	4.0	S	1
2	SMMJ0302+0006	03:02:27.73	+00:06:53.5	1.405	217 ± 9	2.2	O,M?	11.4	0.42	3.6	N	2
3	RGJ0302+0010	03:02:58.94	+00:10:16.3	2.239	55 ± 10	1.7	O,U	9.6	0.38	3.2	N	1
4	RGJ0332–2732	03:32:56.75	–27:32:06.3	2.315	160 ± 20	5.3	O	2.4	0.53	4.4	S	1
5	SMMJ0943+4700*	09:43:04.08	+47:00:16.2	3.351	60	4.7	O,U,M	14.4	0.42	3.2	N	1
6	SMMJ1235+6215	12:35:49.41	+62:15:36.9	2.199	93 ± 6	2.8	O,X,M?	7.8	0.45	3.8	N	2
7	SMMJ1237+6203	12:37:15.97	+62:03:23.1	2.075	179 ± 9	4.6	X,U,B	7.8	0.30	2.5	N	1
8	SMMJ1636+4057	16:36:50.43	+40:57:34.5	2.385	242 ± 11	8.7	O,U,M,B	13.2	0.33	2.7	N	1
9	SMMJ2217+0010	22:17:37.39	+00:10:25.1	(2.610)	179 ± 19	7.9	O,M	3.6	0.40	3.2	N	3
10	SMMJ2217+0017	22:17:42.25	+00:17:02.0	(2.278)	114 ± 27	3.7	O	9.6	0.56	4.7	S	3

Table 1. NOTES:

Column (1): Source ID. Column (2): Source name. Columns (3)–(4): The co-ordinates corresponding to the radio positions from: Ledlow et al. (2002); Swinbank et al. (2004); Chapman et al. (2005); Miller et al. (2008); Morrison et al. (2010); Ivison et al. (2011); Arumugam et al. (in prep); R. J. Ivison (priv. comm). Column (5) The redshifts based on the narrow [O III] emission lines using the galaxy-integrated spectra presented in Fig. 3. For SMMJ2217+0010 and SMMJ2217+0017 we do not detect [O III] and we therefore quote the H α redshift from Takata et al. (2006) and Alaghband-Zadeh et al. (2012), respectively. Column (6): Radio flux densities taken from the same references as for the radio positions. Column (7): Rest-frame radio luminosities using the standard k -correction and a spectral index of $\alpha=0.8$. Column (8): Evidence for AGN activity in the sources on the basis of: O: optical emission-line ratios (Swinbank et al. 2004; Takata et al. 2006; Alaghband-Zadeh et al. 2012; this work); M: excess in the mid-infrared continuum from infrared spectra (Valiante et al. 2007; Menéndez-Delmestre et al. 2009; the evidence for IR-AGN activity in the sources with a “?” is tentative); U: rest-frame UV spectral signatures (Ledlow et al. 2002; Smail et al. 2003; Chapman et al. 2004; Chapman et al. 2005); X: X-ray observations (Alexander et al. 2005); B: Broad-line AGN (Swinbank et al. 2005; Coppin et al. 2008; see Appendix A for more details on the classifications of individual sources). Column (9): The total on-source exposure times for the data presented here. Columns (10)–(11): The average seeing for the observations, based on standard star observations. Column (12): The instrument used for the observations, either SINFONI (S) or NIFS (N). Column (13) A data quality flag as follows: 1: data which have sufficiently high signal-to-noise ratios to study the spatially resolved kinematics; 2: data with lower signal-to-noise ratios and limited spatially resolved information; 3: undetected in [O III] λ 5007 in this study. * For SMMJ0943+4700 we observed the radio counter-part H6 (Ledlow et al. 2002) and the 1.4 GHz flux density has been corrected for an amplification factor of 1.2 (Cowie et al. 2002).

AGN activity (e.g., Kewley et al. 2006), with most of the sources having additional observational evidence for AGN activity (see Table 1 for details); see Appendix A for background information on the individual sources. We provide details of the target selection here.

Seven of our targets are selected from Takata et al. (2006) who presented near-IR spectroscopy around the redshifted [O III] λ 4959,5007 emission-line doublet of 22 high-redshift ULIRGs. In order to select sources that might contain AGN-driven outflows, we chose seven targets with broad (FWHM \gtrsim 700 km s $^{-1}$) and bright ($F_{[\text{O III}]}$ \gtrsim few \times 10 $^{-16}$ erg s $^{-1}$) [O III] emission. We also include in our sample three, $z \approx 2$ –2.5 ULIRGs selected from Alaghband-Zadeh et al. (2012) which were identified as hosting AGN activity on the basis of their rest-frame optical emission-line ratios. These targets were initially selected on the basis of their H α luminosities and are therefore not pre-selected to have luminous and broad [O III] emission. One of the sources was presented in a pilot study (SMMJ1237+6203; Alexander et al. 2010) and we present the whole sample here.

Details of our observations and the targets’ 1.4 GHz flux densities, obtained from the literature, are provided in Table 1. The 1.4 GHz radio luminosities ($L_{1.4\text{GHz}}$) are calculated using Equation (2) from Alexander et al. (2003), with the 1.4 GHz flux densities shown here and an assumed spectral index of $\alpha=0.8$.² We estimate

AGN luminosities for our sources using the SED fitting procedures outlined in §3 and these values are provided in Table 2.

Although this sample is heterogeneous, it is more representative of the overall AGN population than previous IFU studies searching for AGN-driven outflows in high-redshift radio galaxies (with $L_{1.4\text{GHz}} \gtrsim 10^{27} \text{ W Hz}^{-1}$; e.g., Nesvadba et al. 2008). For example the radio luminosities of our sources ($L_{1.4\text{GHz}}=10^{24}$ – $10^{25} \text{ W Hz}^{-1}$) imply a space density of $\Phi \approx 10^{-5} \text{ Mpc}^{-3}$ compared to $\Phi \lesssim 10^{-8} \text{ Mpc}^{-3}$ for high-redshift radio galaxies (Fig. 1; Simpson et al. 2012; Willott et al. 1998). This is important if we are to understand the prevalence of AGN-driven outflows in high-redshift galaxies. In Fig. 1 we compare the integrated [O III] properties and radio luminosities of our sample with low- and high-redshift AGN.

2.2 Gemini-North NIFS observations

Seven of the sources in our sample (those selected from Takata et al. 2006) were observed using Gemini-North NIFS (Table 1). The NIFS IFU uses an image slicer to reimage a 3.0×3.0 arcsec 2 field into 29 slices of width 0.103 $''$ with a pixel scale of 0.04 $''$ along the slices. The dispersed spectra from the slices are reformatted on the detector to provide two-dimensional spectro-imaging. Depending on the target redshift, we used the J –, H – or K –band grisms to ensure that we cover the rest-frame [O III] λ 4959,5007 emission-line doublet. These grisms have an approximate spectral resolutions of $\lambda/\Delta\lambda \approx 6040$, 5290 and 5290, respectively (FWHM \approx 2, 3, 4 Å, or $\Delta v \approx$ 50, 57, 57 km s $^{-1}$). For our analysis we measured the instrumental dispersion more accu-

² This value is approximately the mean value for radio-identified SMGs with an observed range of roughly $\alpha=0.2$ –1.5, which includes AGN (Ibar et al. 2010). Here we define a spectral index α such that flux density, S_ν , and frequency, ν , are related by $S_\nu \propto \nu^{-\alpha}$.

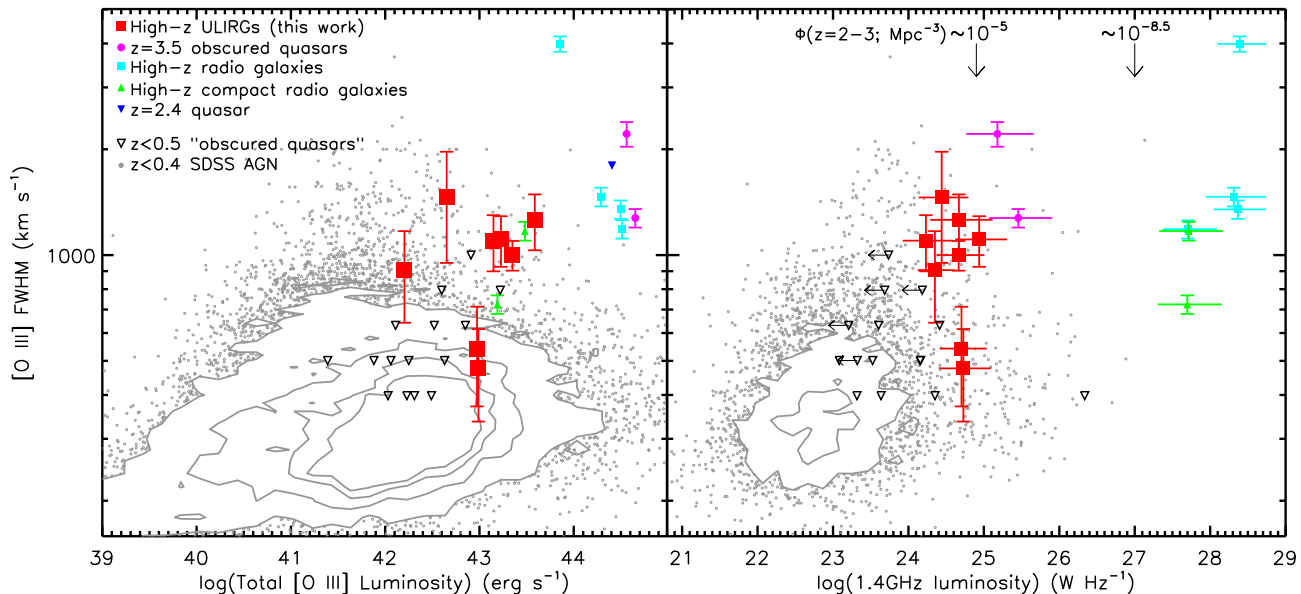


Figure 1. FWHM versus total [O III] λ 5007 luminosity (*left*) and FWHM versus 1.4GHz luminosity (*right*) for our eight [O III] detected targets. Shown for comparison are low redshift ($z < 0.4$) AGN from the Sloan Digital Sky Survey (Mullaney et al. in prep) and $z < 0.5$ obscured quasars with long-slit data (Greene et al. 2011). Also shown are other high-redshift sources with IFU data: $z \approx 2-3$ radio galaxies (Nesvadba et al. 2006, 2008), compact radio galaxies (Nesvadba et al. 2007a), $z \approx 3.5$ obscured quasars (Nesvadba et al. 2011) and a $z = 2.4$ quasar (Cano-Díaz et al. 2012). Our targets have very broad [O III] emission, comparable with high-redshift radio galaxies but having 3–4 orders of magnitude lower radio luminosities such that they are ≈ 3 orders of magnitude more common at $z \approx 2-3$. When the [O III] profile is decomposed into multiple components, the FWHMs of the broadest components have been plotted. All rest-frame radio luminosities are calculated using the standard k -correction, on the basis of their measured 1.4GHz flux densities. Radio spectral indices are taken to be $\alpha = 0.8$; however, the horizontal error bars indicate the range of luminosities using spectral indices in the range $\alpha = 0.2-1.5$. The arrows in the right panel correspond to space densities of $\Phi \approx 10^{-5} \text{ Mpc}^{-3}$ (Simpson et al. 2012) and $\Phi \approx 10^{-8.5} \text{ Mpc}^{-3}$ (Willott et al. 1998) from the radio luminosity function at $z \approx 2.5$.

rately, by measuring the widths of several bright sky-lines close to the observed wavelengths of the emission lines for the observations of each source. We found that the uncertainties in the instrumental dispersion (by measuring the scatter from the widths of several sky-lines) to be insignificant ($\approx 5\%$) compared to the uncertainties from our fitting procedures. We consequently do not include the uncertainties on the instrumental resolution in our measurements. These observations were taken between 2008 March 25 and May 19 and 2009 August 5 and December 30. All observations were taken in $< 0.5''$ seeing.

The observations were performed using repetitions of the standard ABBA configuration in which we chopped either $6''$ to blank sky or, if the source was compact (emission-line region $< 1.5''$), we chopped within the IFU. Individual exposures were 600s. Final on-source exposure times and seeing measurements, calculated using the corresponding standard star observations, are shown in Table 1.

We reduced the data with the Gemini IRAF NIFS pipeline which includes sky subtraction, wavelength calibration, and flat fielding. Attempts to remove residual OH sky emission lines were made using the sky-subtraction techniques described in Davies (2007). We further corrected for variations in the night sky emission by masking the source (when clearly detected) and taking a median of each pixel-column and consequently subtracting the (empty sky) background separately from each wavelength.

2.3 VLT SINFONI observations

Three of the sources in our sample were observed using VLT SINFONI (Table 1). The full details of these SINFONI observations are given in Alaghband-Zadeh et al. (2012) with only ba-

sic information given here. We used the widest available field-of-view, $8.0 \times 8.0 \text{ arcsec}^2$, which is divided into 32 slices of width $0.25''$ with a pixel scale $0.125''$ along the slices. The $H+K$ grating was used, which gives an approximate resolution of $\lambda/\Delta\lambda \approx 1500$ (FWHM $\approx 13 \text{ \AA}$ or $\Delta v \approx 200 \text{ km s}^{-1}$). We made accurate measurements of the instrumental dispersion for the observations for each source in the same manner as outlined for the NIFS observations in the previous section. Again we found the uncertainties on the instrumental dispersion to be insignificant compared to the uncertainties from our fitting procedures. The targets were chopped around quadrants of the IFU for sky subtraction. All observations were taken in $< 0.6''$ seeing. Individual exposures were 600s. Final on-source exposure times and seeing measurements, calculated using the corresponding standard star observations, are shown in Table 1.

The data were reduced using the SINFONI ESOREX pipeline, which includes sky subtraction, wavelength calibration and flat fielding.

2.4 Flux calibration and stacking

Each night's data were flux calibrated separately using observations of standard stars, at a similar airmass to the target galaxies, which were reduced in the same manner as the targets. Since the [O III] $\lambda\lambda$ 4959,5007 emission-line doublets typically lie in regions of $> 95\%$ sky transparency, no corrections were made for telluric absorption. To find spatial centroids for the flux-calibrated data cubes, white light (wavelength collapsed) images around the redshifted [O III] λ 5007 emission line (NIFS targets) or H α emission line (SINFONI targets) were produced. The data cubes for which we could not measure a centroid were discarded to improve the

reliability of the spatially resolved data. Data cubes were only discarded for SMMJ0302+0006 (2 discarded out of the 21 observed), RGJ0302+0010 (4 discarded out of 20) and SMMJ1235+6215 (8 discarded out of 21). We then spatially aligned and co-added the individual data cubes to create the final mosaic, using a median with a 3σ clipping threshold to remove remaining cosmetic defects and cosmic rays. The total on-source exposure times used in the final stacks are given in Table 1.

In all of the following sections, the effect of instrumental dispersion was corrected for by subtracting it in quadrature from the observed line dispersions.

3 STAR-FORMATION RATES AND AGN LUMINOSITIES

To assist in the analyses of this work we need to constrain the star-formation rates and AGN luminosities of the eight [O III]-detected sources in a consistent manner. To achieve this we obtained infrared flux densities from the literature (Table 2) and fit these data using AGN and star-forming galaxy templates with the χ^2 minimisation spectral energy distribution (SED) fitting procedure outlined in Del Moro et al. (2012). Briefly, we fit the infrared data using the empirical AGN template defined in Mullaney et al. (2011), allowing for $A_V=0-5$ mag of extinction, with each of the “SB2”–“SB5” star-forming galaxy templates; the “SB1” star-formation template did not fit the data well in any of the sources. This provides four best-fitting solutions (i.e., one for each of the four star-forming galaxy templates) with minimum χ^2 solutions. We used these solutions to find the star-formation rates and AGN luminosities for each of the sources using the methods described below. The infrared data points and the overall best-fit solutions are shown in Fig. 2.

We found convincing evidence for both star formation and AGN activity at infrared wavelengths for all of the sources except for RGJ0302+0010 (for which there is insufficient infrared data available) and SMMJ0217–0503, which had no significant AGN component providing only an upper limit on the AGN infrared luminosity. The AGN components in SMMJ0943+4700 and SMMJ1237+6203 were found to be particularly bright and dominated the mid-infrared emission; the SED fitting results for SMMJ0943+4700 also agreed well with that found from mid-IR spectral fitting (Valiante et al. 2007) but no mid-IR spectroscopy exists for SMMJ1237+6203. The AGN components for the other sources are weaker at mid-IR wavelengths. However, three of the sources have published mid-infrared spectroscopy (SMMJ0302+0010, SMMJ1235+6215, and SMMJ1636+4057; Menéndez-Delmestre et al. 2009), and we found good agreement between the strength of the AGN component calculated from our SED-fitting procedure and the strength of the AGN derived from the mid-infrared spectroscopy.

We used the SED-fitting results to calculate the infrared luminosities of the star-formation components ($L_{\text{IR,SF}}$; integrated over 8-1000 μm) and consequently calculated star formation rates following Kennicutt (1998); see Table 2. This was achieved by taking the mean luminosity of the best-fitting solutions that used the four star-formation templates described above. The quoted uncertainties in the star-formation luminosity and star-formation rates are the average of the difference between these mean values and the models with the highest and lowest values. We found that all of the sources have $L_{\text{IR,SF}} > 10^{12} L_{\odot}$, confirming that they are ULIRGs with SFRs in the range $\approx 300-1400 M_{\odot} \text{ yr}^{-1}$. For the source RGJ0302+0010 we estimated the infrared luminosity using the radio-infrared relationship for star-forming galaxies (e.g.,

Helou et al. 1985) with $q = 2.1$, which is a typical value for high-redshift ULIRGs (Kovács et al. 2006). For this source we take the value of $L_{\text{IR,SF}}$ as an upper limit because the AGN will be contributing some unknown fraction of the radio luminosity (e.g., see Fig. 2 which shows that some of the sources have excess radio emission relative to that expected from star-formation alone; also see Del Moro et al. 2012).

To determine the bolometric AGN luminosities for each source we first calculated the AGN continuum luminosity [rest-frame $\nu L_{\nu}(6\mu\text{m})$] by taking the average AGN contribution to the $6\mu\text{m}$ flux of the four models described above. These average infrared AGN luminosities are then converted into AGN bolometric luminosities using the $6\mu\text{m}$ -to-2–10 keV luminosity relationship found for AGNs (conversion factor of ≈ 0.3 ; Lutz et al. 2004) and the 2–10 keV-to-bolometric luminosity ratio in Elvis et al. (1994) (conversion factor of ≈ 25 ; see Table 2). This overall correction factor of 7.5 that we apply to convert between $\nu L_{\nu}(6\mu\text{m})$ and AGN bolometric luminosity is in excellent agreement with the correction factor of $\approx 8 \pm 2$ found by Richards et al. (2006) from their mean SED of SDSS quasars. We found that the two sources with the largest fractional uncertainties on their SED-derived AGN luminosities are also those which only have tentative evidence for IR-AGN activity in their mid-infrared spectra (see Table 2). However, we compared all the SED-derived AGN bolometric luminosities to those predicted using the measured [O III] luminosities and the locally derived relationship of Heckman et al. (2004) ($L_{\text{AGN}}=3500L_{[\text{OIII}]}$). We found that the $L_{[\text{OIII}]}$ derived AGN luminosities are on average a factor of ≈ 2.5 higher than the SED derived values, with a remarkably small scatter (all sources have a factor of 2.5 ± 1.5), giving evidence that (1) our derived AGN bolometric luminosities are reasonable, and (2) the [O III] luminosities are dominated by AGN activity. To predict the AGN luminosity for the source RGJ0302+0010, for which we were unable to perform the SED fitting, we therefore take the $L_{[\text{OIII}]}$ derived AGN luminosity and divide by a factor of 2.5 (see Table 2).

4 ANALYSIS AND RESULTS

We have studied the galaxy-integrated and spatially resolved properties of the [O III] $\lambda\lambda 4959,5007$ emission-line doublet in our sample. Of the ten sources in our sample, six have spatially extended [O III] emission, two have lower quality [O III] data and limited spatially-resolved information and two were undetected in [O III] (see Table 1). In this section we provide the details of our analyses and give an overview of the results of the sample as a whole. We give specific results for individual sources in Appendix A. In this section we first describe the galaxy-integrated properties of the eight [O III] detected targets before providing a detailed analysis of the kinematics for the six spatially resolved sources. We defer discussion of the results and their implications for galaxy evolution to §5.

4.1 Galaxy-integrated spectra

In Fig. 3 we show the galaxy-integrated spectra around the [O III] $\lambda\lambda 4959,5007$ emission-line doublet for the eight sources with detected [O III] emission. The two sources that have an [O III] flux below our detection threshold (SMMJ2217+0010 and SMMJ2217+0017; see Appendix A9 and A10) are not shown. The spectra were created by integrating over the full spatial extent of the observed [O III] line emission; i.e., the aperture sizes to create the

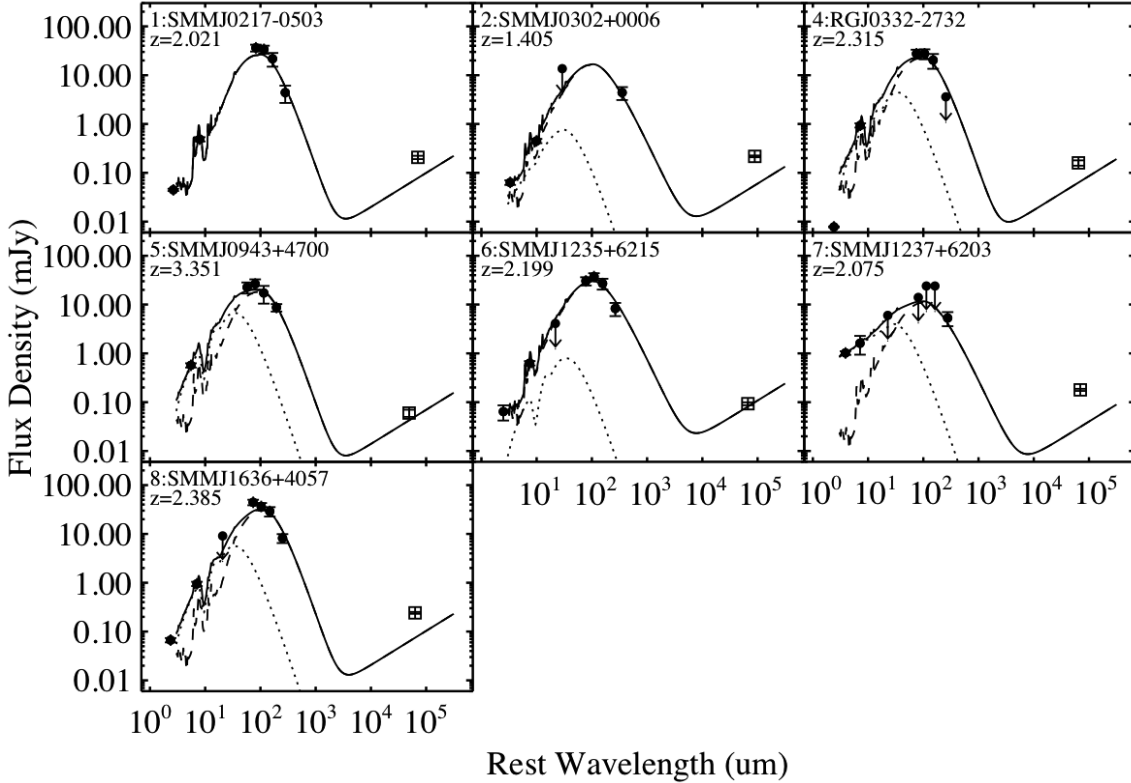


Figure 2. The infrared flux densities (filled circles) in the rest frame for the seven sources for which we performed SED fitting (see §3, Table 2 and Del Moro et al. 2012 for more details). The source RG 0302+0010 (source ID number 3) does not appear due to insufficient infrared data available. For guidance, also shown are the overall best-fit SEDs. The total SEDs are shown as solid curves, the AGN templates are shown as dotted curves and the starburst templates are shown as dashed curves. The 1.4 GHz flux densities (open squares) were not included in the SED fitting process. The source RG J0302+0010 does not appear due to insufficient available infrared data. These SED fits were used to constrain the contributions to the infrared luminosities from AGN activity and star formation activity for each of the sources (Table 2).

spectra were chosen by increasing the sizes until the [O III] fluxes reached a maximum.

To fit the emission-line profiles we employed a χ^2 minimisation procedure, down-weighting at the positions of the strongest sky lines. We fit the [O III] $\lambda\lambda$ 4959,5007 emission-line doublet with Gaussian components using a fixed wavelength separation. The intensity ratio was fixed at [O III] λ 4959/[O III] λ 5007=0.33 (e.g., Dimitrijević et al. 2007) and the width of the [O III] λ 4959 line was fixed to be the same as the [O III] λ 5007 line. In several cases the emission-line profiles are complex, with the presence of asymmetric wings. To characterise this complexity, we first fit a single Gaussian profile followed by a double Gaussian profile, only accepting the double Gaussian profile if it resulted in a significant improvement ($\Delta\chi^2 > 25 \sim 5\sigma$). In one source, SMMJ1636+4057, we find evidence for a third Gaussian component at +1350 km s⁻¹ from the narrow component; we confidently attribute this to [O III] as there are other emission lines found at the same velocity as this component (Smail et al. 2003; also see Appendix A8). Uncertainties on the parameters are calculated by perturbing one parameter at a time, allowing the others to find their optimum values, until the χ^2 value increases by 1. The mean of these upper and lower uncertainties are quoted throughout. The parameters for all of the fits and their uncertainties are given in Table 3. We note that the true absolute uncertainties on the flux measurements will be a factor of ≈ 2 –3 higher, due to unknown uncertainties on the absolute flux calibrations. We note that there are some discrepancies between

the fluxes shown here and those given in Takata et al. (2006) and Alexander et al. (2010). We attribute this to the more reliable flux calibration procedures used in our work.

In Fig. 3 it can be seen that the [O III] emission-line profiles are diverse across the sample, with both narrow (FWHM \approx few hundred km s⁻¹) and broad components (FWHM \approx 900–1500 km s⁻¹) which can be blueshifted and/or redshifted with respect to the narrow emission ($-350 \lesssim \Delta v \lesssim 1350$ km s⁻¹). We will discuss in §5.1 that the narrow [O III] components are likely to be tracing the host galaxy dynamics and merger remnants while the broad components are most likely due to energetic outflows (see Appendix A for a discussion on individual objects). We will also argue that the observed diversity across the sample is due to a combination of orientation and obscuration effects.

The four sources for which we were able to decompose the line profiles into multiple Gaussian components are those which have the highest flux and consequently highest signal-to-noise (Table 3). It is possible that the other four detected sources also have both narrow and broad emission line components but we were unable to decompose them in these spectra due to their lower signal-to-noise ratios. For example, in one source (SMMJ0217–0503), we identify a broad [O III] component in a sub-region of the IFU datacube that is not identified in the galaxy-integrated spectrum (§4.3).

In the following sections we discuss the spatially re-

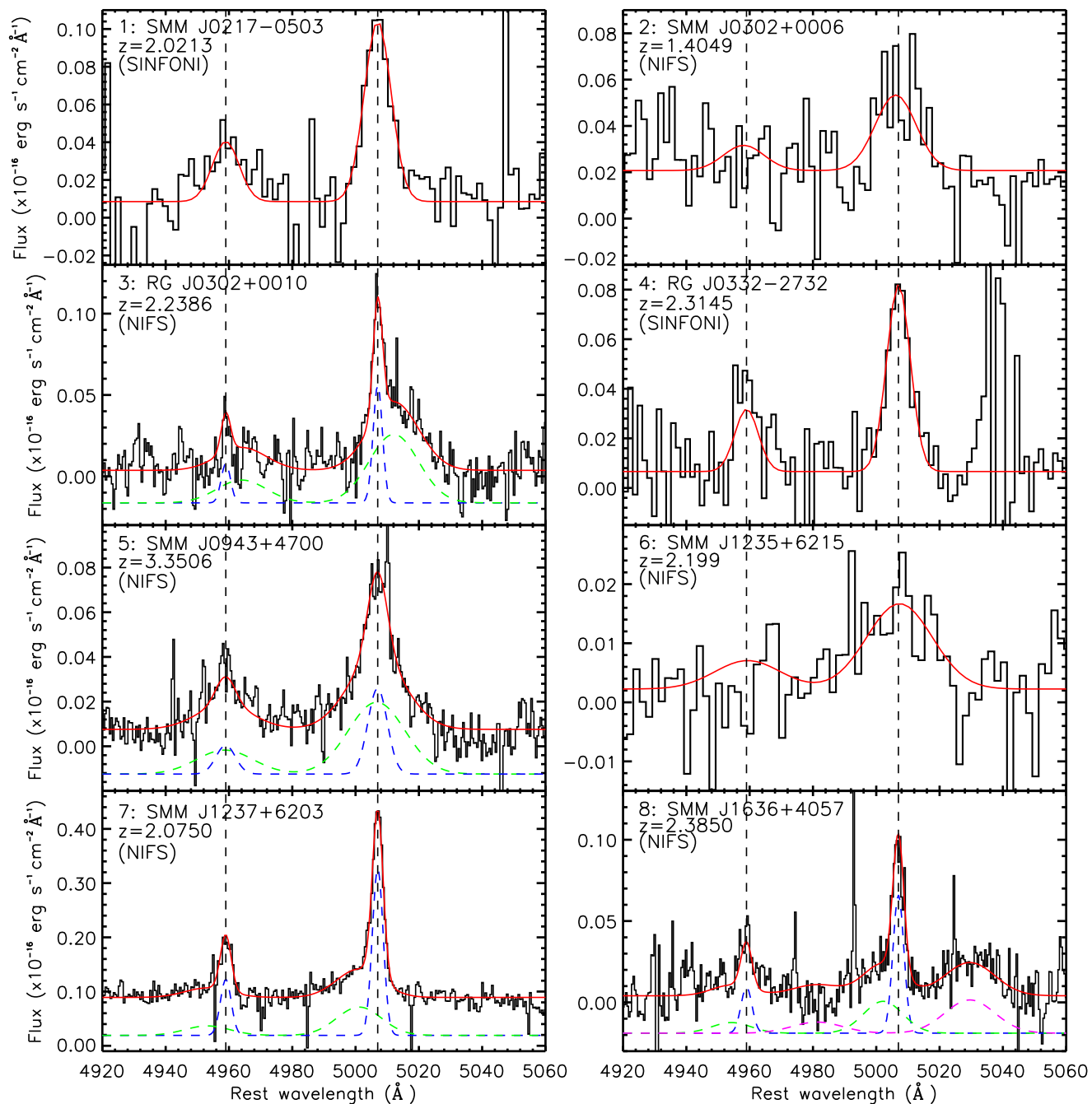


Figure 3. Galaxy-integrated spectra, shifted to the rest-frame, around the $[\text{O III}]\lambda\lambda 4959, 5007$ emission-line doublet. A large variety in the $[\text{O III}]$ emission-line profiles are found with both blueshifted and redshifted extremely broad ($\text{FWHM} \approx 900\text{--}1500 \text{ km s}^{-1}$) emission-line components, in addition to narrow emission-line components. Of particular note is SMM J1636+4057 which exhibits two broad components separated by $\approx 1700 \text{ km s}^{-1}$, one blueshifted and one redshifted with respect to the narrow component (see Appendix A8 for details). The dashed curves show the individual Gaussian components (with an arbitrary flux offset) of the fits when two or three components are required. The solid curves show the best fitting overall emission-line profiles. The vertical dashed lines show the rest-frame wavelengths of redshifted $[\text{O III}]\lambda 4959$ and $[\text{O III}]\lambda 5007$ based on the redshift of the narrowest Gaussian component. The spectra for SMM J0302+0006 and SMM J1235+6215 are of lower signal-to-noise than the other spectra and have been binned by a factor of four for clarity. The parameters of the emission-line fits and their uncertainties are given in Table 3.

solved properties of all of the $[\text{O III}]$ detected sources except SMM J0302+0006 and SMM J1235+6215. SMM J0302+0006 is spatially unresolved in our data while SMM J1235+6215 only displays tentative evidence for extended emission (see Appendix A2 and A6 for further details on these two sources). Due to the low signal-to-noise ratios of the data for these two sources it is difficult

to determine if they are intrinsically compact or if any extended emission lies below our detection threshold. We do not discuss these two sources any further in this section.

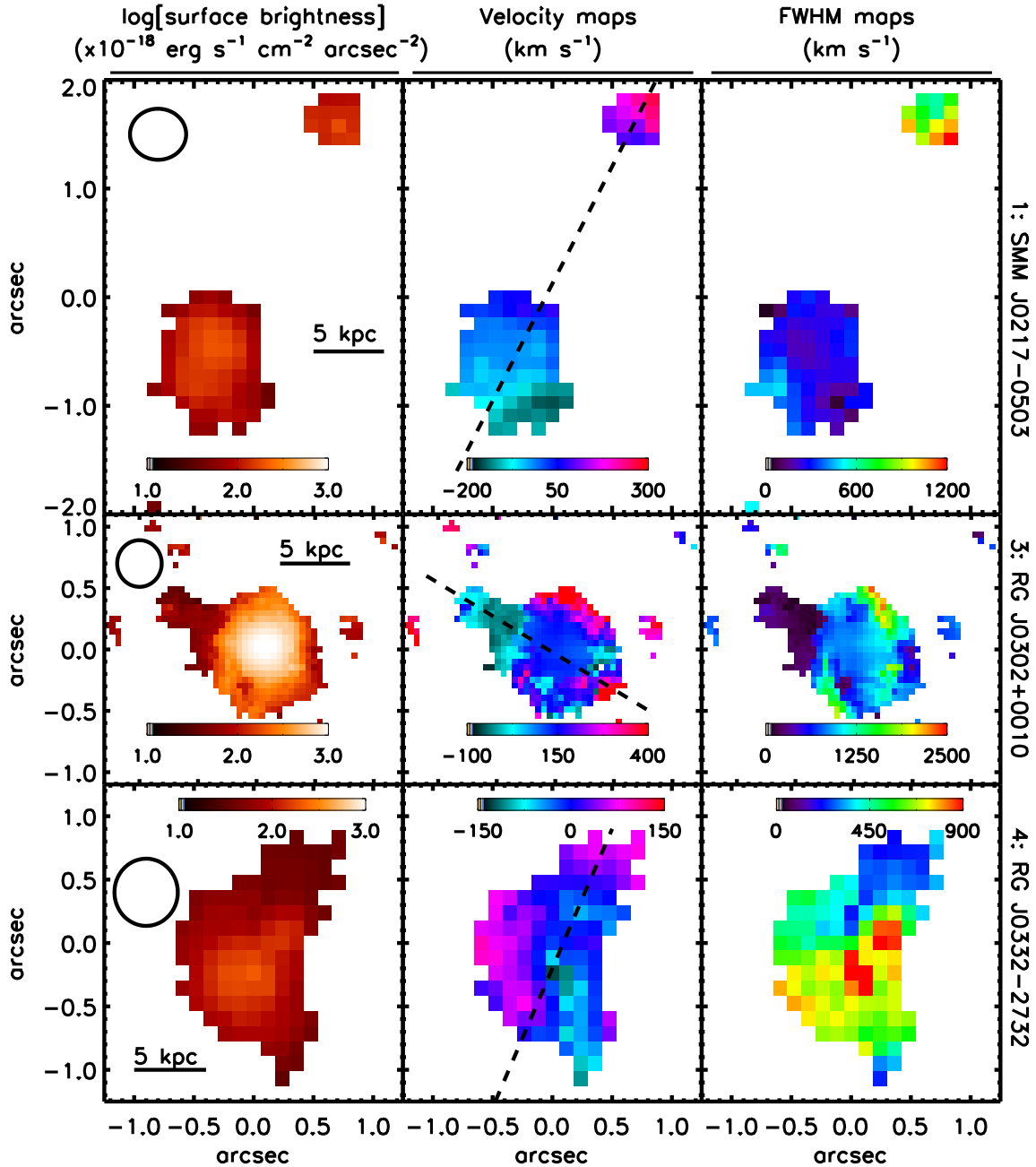


Figure 4. [O III] flux, velocity and FWHM fields, from fitting single Gaussian components to individual pixels for our six sources with spatially resolved emission. The [O III] emission is evidently very diverse and complex with large velocity offsets (up to $\approx 1700 \text{ km s}^{-1}$) and regions of both narrow (FWHM \approx few 100 km s^{-1}) and broad (FWHM $\approx 700\text{--}2500 \text{ km s}^{-1}$) emission-line components. We attribute the narrow emission to galaxy dynamics and merger remnants and the broad emission to energetic outflows. Zero velocity is defined as the redshift of the narrowest component shown in the galaxy-integrated spectra (Fig. 3). No corrections have been made for unknown orientation effects or dust extinction. The open circles denote the average seeing disc during the observations of each target and the solid bars indicate 5 kpc in extent. The dashed lines show the axes through which we produced the velocity and FWHM profiles shown in Fig. 6. North is up and east is left in all panels.

4.2 Flux, velocity and FWHM maps

In Fig. 4 we show flux maps, velocity fields and FWHM maps for the six sources for which we were able to spatially resolve the [O III] emission. These maps were produced using an adaptive binning technique such that the high surface brightness regions are averaged over smaller regions than the outer low surface brightness regions. We do this by taking a mean spectrum

over 3×3 spatial pixels, increasing to 5×5 pixels (maximum for SINFONI data) and ultimately to 7×7 pixels (maximum for NIFS data) if the signal was too low to produce a sufficiently high χ^2 improvement in a continuum+emission-line fit over a simple continuum fit ($\Delta\chi^2 > 16$; equivalent to $\approx 4\sigma$). The continuum level was taken to be the median of line-free continuum in the vicinity of the emission-lines. When this criterion is met, we fit the [O III] $\lambda\lambda 4959, 5007$ emission-line doublet with a single-Gaussian

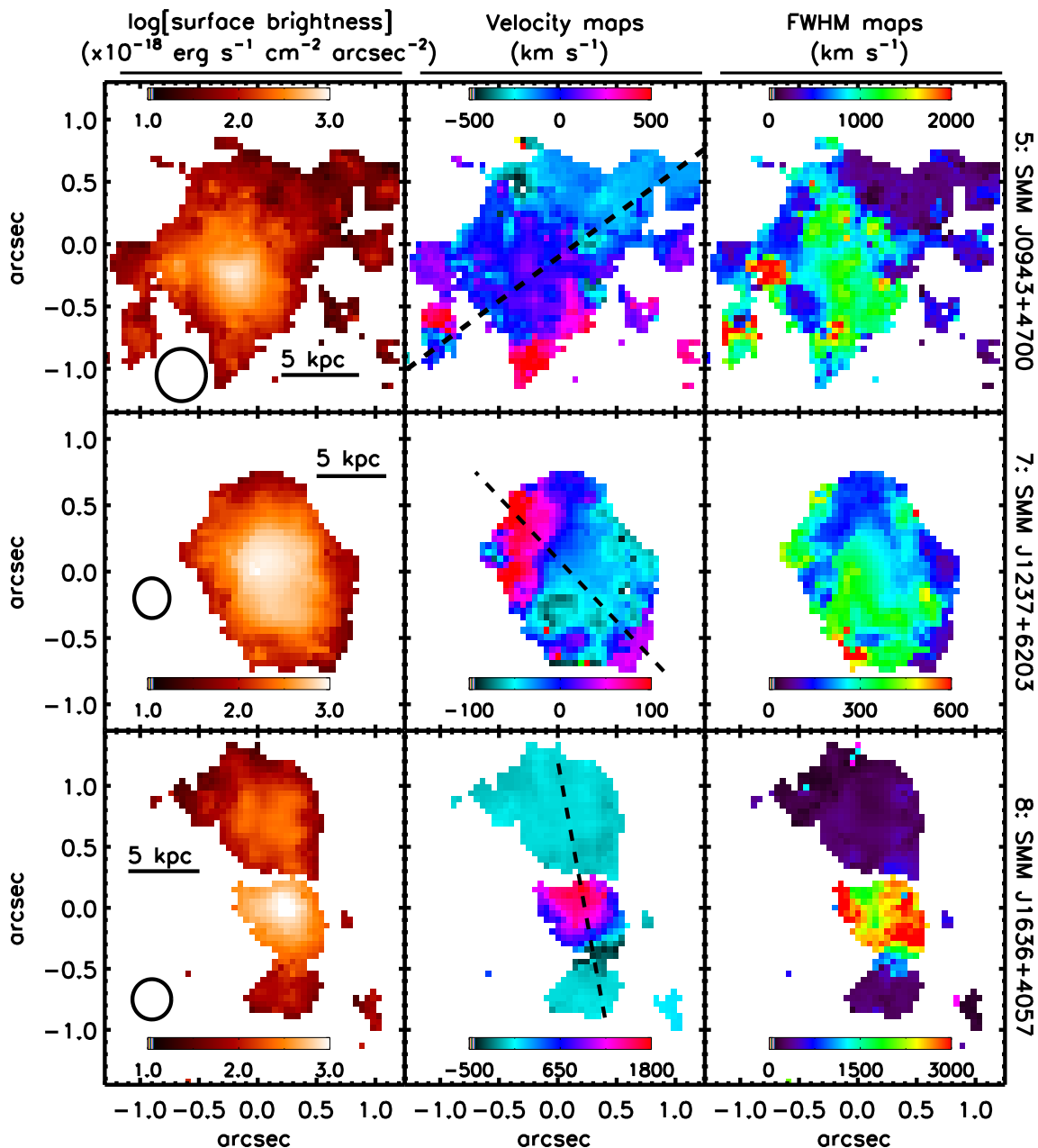


Figure 4. continued.

profile, allowing the normalisation, width and central wavelength to vary. We defined zero velocity at the central wavelength of the narrowest Gaussian component in the galaxy-integrated spectra.

The flux maps in Fig. 4 show that the observed emission-line regions of these sources are diverse and irregular, with at least two sources showing spatially distinct emission-line regions, indicating multiple interacting or merging systems (SMMJ0217–0503 and SMMJ1636+4057). The [O III] emission is observed to be extended up to ≈ 20 kpc. The velocity fields and FWHM maps in Fig. 4 show that there are regions dominated by narrow [O III] emission (\approx few hundred km s⁻¹) with modest velocity gradients ($\Delta v \lesssim 200$ km s⁻¹). There are also regions which are kinematically chaotic, extended up to 15 kpc in spatial extent, with extreme

widths ($700 \lesssim \text{FWHM} \lesssim 2500$ km s⁻¹) and large velocity offsets (Δv up to ≈ 1700 km s⁻¹).

The velocity fields and FWHM maps in Fig. 4 were created using single Gaussian components and do not separately trace the broad and narrow [O III] emission line components observed in the galaxy-integrated spectra (Fig. 3). Instead they roughly trace the brightest [O III] kinematic component. For example, we will show that although the source SMMJ1237+6203 looks to have fairly quiescent kinematics in Fig. 4, the extremely broad and high-velocity [O III] component seen in the galaxy-integrated spectrum (FWHM ≈ 1000 km s⁻¹; $\Delta v \approx -350$ km s⁻¹; Fig. 3) is found over the central 5–8 kpc (see also Alexander et al. 2010). In the follow-

ing sections, we therefore use further analysis methods to give a more complete description of the kinematics of these sources.

4.3 Regions dominated by narrow and broad emission lines

In Fig. 5 we show spatially-integrated spectra from regions dominated by broad or narrow emission lines. To produce these spectra we took our [O III] FWHM maps (Fig. 4) and integrated the spectra over the pixels that have $\text{FWHM} < 500 \text{ km s}^{-1}$ (narrow [O III]) and those that have $\text{FWHM} > 500 \text{ km s}^{-1}$ (broad [O III]). We do not do this for SMM J1237+6203 as there are too few pixels that contain emission lines with $\text{FWHM} > 500 \text{ km s}^{-1}$. For this source the narrow component of the [O III] emission line seen in Fig. 3 dominates the whole of the velocity and FWHM maps. The value of 500 km s^{-1} was motivated by the maximum line-widths generally expected from galaxy dynamics and merger remnants in high-redshift ULIRGs (see §5.1; Alaghband-Zadeh et al. 2012). We fit the spectra using the same method as the galaxy-integrated spectra (see § 4.1) and provide all of the parameters of the fits and their uncertainties in Table 4. We also fit any observed H β emission in these regions using a single Gaussian profile and give the parameters and their uncertainties in Table 4. When no H β emission lines were detected we use the standard deviation of the emission-line free continuum and the FWHM of the [O III] emission-line components to derive 3σ upper limits on the flux.

By comparing the spatially-integrated spectra from the regions shown in Fig. 5 with the galaxy-integrated spectra shown in Fig. 3 we are able to locate the different kinematic components in the galaxies. For example, in the majority of the sources there is narrow emission ($\text{FWHM} \approx$ a few 100 km s^{-1}) extended over the full spatial extent of the emission-line regions (up to $\approx 20 \text{ kpc}$). The regions dominated by the broadest emission lines (Fig. 5) are also the regions where the [O III] emission peaks in surface brightness and the [O III]/H β ratios are the largest ($\log([\text{O III}]/\text{H}\beta) > 0.6$; see Table 4), indicating excitation dominated by AGN activity in these regions (e.g., Kewley et al. 2006). Further evidence for the broad emission lines being associated with AGN activity is found in the source SMM J0217–0503, which is comprised of two separate systems, and the broad emission line is only observed in the system that is identified as hosting AGN activity by Alaghband-Zadeh et al. (2012) (also see Appendix A1). In addition, SMM J1636+4057 displays two broad [O III] components which are co-spatial with the H α broad-line region of the AGN (Menéndez-Delmestre et al. 2012; see Appendix A8).

4.4 Velocity profiles

To further quantify the [O III] velocity structure and spatial extents of the different kinematic components in our sample we created velocity and FWHM profiles for each of the six spatially resolved sources and show them in Fig. 6. To produce these profiles we first repeated the pixel-by-pixel fitting routine outlined in §4.2 with the addition of allowing a second Gaussian component to be fit at each pixel, if this resulted in a significant improvement ($\Delta\chi^2 > 16$; equivalent to $\gtrsim 4\sigma$) over a single Gaussian component. Only two of the sources (RG J0302+0010 and SMM J1237+6203) had sufficiently bright narrow and broad [O III] emission-line components to de-compose the profiles using this method. For these two sources we took these double-Gaussian component FWHM and velocity maps and took a running median of all the pixels orthogonal to a vector through the most extended emission

(see dashed lines in Fig. 4). For the other four spatially resolved sources (SMM J0217–0503; RG J0332–2732; SMM J0943+4700 and SMM J1636+4057) we used the single-Gaussian component FWHM and velocity maps shown in Fig. 4. For the sources SMM J0217–0503 and RG J0332–2732 we also plot the relative velocities of the H α emission, extracted from the regions shown in Fig. 5, on these velocity profiles. For the source SMM J1636+4057 we plot the [O III] FWHM and velocity offset values from the spectra extracted from the broad [O III] region (Fig. 5) and H α and CO(1–0) data from the literature (Swinbank et al. 2005; Ivison et al. 2011; Menéndez-Delmestre et al. 2012; see Appendix A8 for more details).

Fig. 6 enables us to separately trace the kinematics of the narrow ($\text{FWHM} \approx$ a few hundred km s^{-1}) and broad ($\text{FWHM} \approx 700\text{--}1400 \text{ km s}^{-1}$) [O III] emission-line components. The narrow emission lines have small velocity gradients ($\Delta v \lesssim 200 \text{ km s}^{-1}$) and appear to be at roughly the same velocity as the H α emission and molecular gas, when these data are available for comparison. In contrast, the broad components are offset from the narrow emission by $|\Delta v| \approx 150\text{--}1400 \text{ km s}^{-1}$ and are found over $\approx 4\text{--}15 \text{ kpc}$ in observed linear extent (except SMM J0217–0503 for which the broad emission is spatially unresolved; $\leq 4 \text{ kpc}$). The source RG J0332–2732 has emission that is not clearly separated into broad and narrow components; however, we note that the emission is broadest ($\text{FWHM} \approx 700 \text{ km s}^{-1}$) in the brightest central region. The source SMM J0217–0503 consists of two separate systems, which are indicated in Fig. 6. In the northern system we do not observe any narrow emission lines; however, the [O III] emission has a large velocity offset from the peak in the H α emission ($\Delta v = -460 \pm 60 \text{ km s}^{-1}$; see Appendix A1 for further details). Of particular note is the source SMM 1636+4057 for which the broad components are found at $v \approx \pm 850 \text{ km s}^{-1}$ from the systemic velocity of the the H α broad-line region of the AGN (Swinbank et al. 2005; Menéndez-Delmestre et al. 2012; see Appendix A8).

Due to the large uncertainties in the velocity offsets and FWHM of the broad [O III] components, we do not interpret their kinematic structure any further than quoting their spatial extent and velocity offsets from the systemic redshifts. However, we did perform tests to ensure that the broad emission lines are truly spatially extended and that the observed extents are not just the result of intrinsically compact regions being extended by the seeing during our observations. Following Alexander et al. (2010) we did this by extracting spectra from different regions and we found velocity structure in the broad emission lines, confirming that they are spatially extended (see Appendix A for details on individual sources).

For the remainder of this work we quote the spatial extent of the broad [O III] emission as the extent of the broad [O III] regions shown in Fig. 5 (see Table 4). These values are consistent, within the quoted uncertainties, with spatial extents of the broad [O III] emission found in the velocity profiles shown in Fig. 6. The source SMM J1237+6203 does not appear in Fig. 5 (see §4.3), we therefore take the spatial extent from Fig. 6 ($\approx 5 \text{ kpc}$) which is conservative based on the $4\text{--}8 \text{ kpc}$ extent found by Alexander et al. (2010) for this source. The quoted spatial extents are likely to be lower limits as they are not corrected for orientation and low surface brightness broad [O III] emission will not be detected by our fitting procedures (described in §4.2). We define the velocity offsets of the broad emission lines from the systemic, as the velocity differences between the broad and narrow [O III] emission lines in the spectra extracted from the broad [O III] regions (see Fig. 5 and Table 4). For SMM J0217–0503 and RG J0332–2732 we use the velocity offset to the narrow H α emission, as no narrow [O III] emission

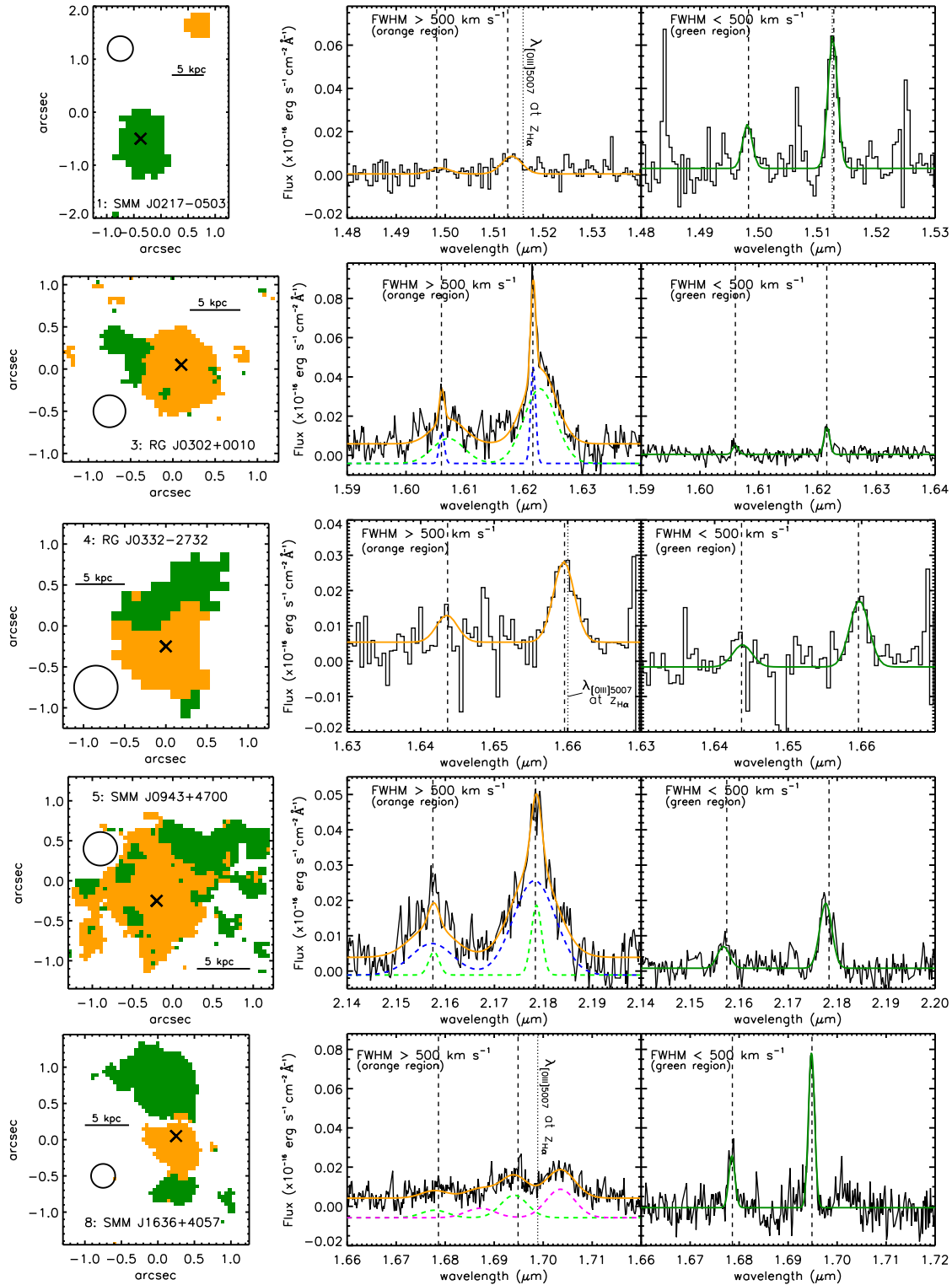


Figure 5. *Left:* Maps of our spatially resolved sources colour-coded to separate regions dominated by narrow [O III] emission lines (green: FWHM $< 500 \text{ km s}^{-1}$) or broad [O III] emission-lines (orange: FWHM $> 500 \text{ km s}^{-1}$) determined from the FWHM maps shown in Fig. 4. For the source SMMJ1237+6203 the narrow component dominates the [O III] flux throughout and therefore we are unable to define the separate spatial regions using this method (see §4.3 for details). The narrow emission lines are observed over the largest extents but the broad emission lines are still observed in extended regions ($\approx 4\text{--}15 \text{ kpc}$). The open circles denote the average seeing discs during the observations, the solid bars indicate 5 kpc in extent and the crosses indicate the peak in [O III] flux. North is up and east is left. *Middle and Right:* The spatially-integrated spectra around the [O III] $\lambda\lambda 4959, 5007$ emission-line doublet extracted from the regions indicated in the left panels. The central regions exhibit complex emission-line profiles. The dashed curves show the individual Gaussian components (with an arbitrary flux shift) of the fits when two components were required. The solid curves show the best fitting overall emission-line profiles; the parameters and their uncertainties are shown in Table 4. The vertical dashed lines shows the centroids of the [O III] $\lambda\lambda 4959, 5007$ narrow line components in the galaxy-integrated spectra (Fig. 3). The vertical dotted lines for SMMJ0217-0503 and RGJ0332-2732 show the expected position of [O III] given the redshift of the H α emission-line from the same spatial region (Alaghband-Zadeh priv. comm.). For the source SMMJ1636+4057 the vertical

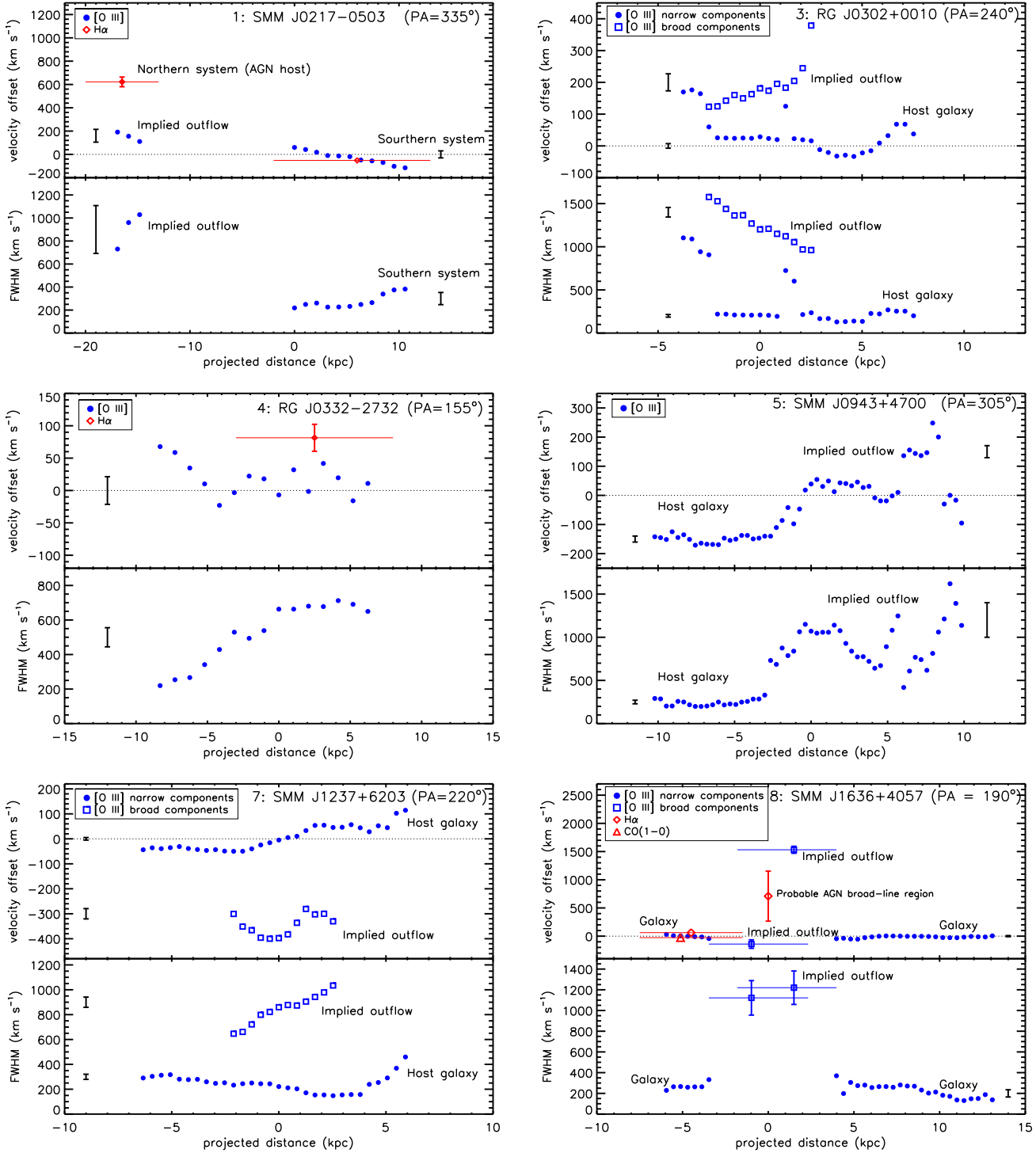


Figure 6. A velocity and FWHM profile of the [O III] emission lines for our six spatially resolved sources, along vectors at the angles indicated in the upper-right of each panel (see §4.4 for how these were produced). When it was possible to de-couple the [O III] emission-line profiles into two components we have shown these as filled circles (narrow) and open squares (broad). In some cases H α data and CO(1–0) data are plotted, taken from the literature (Swinbank et al. 2005; Ivison et al. 2011; Alaghband-Zadeh et al. 2012; Menéndez-Delmestre et al. 2012). The data points for the broad [O III] components for the source SMM J1636+4057 are taken from the fits to the spectra shown in Fig. 5. In all cases there are underlying narrow [O III] emission lines (FWHM \approx few hundred km s $^{-1}$) with small velocity gradients ($\Delta v \lesssim 200$ km s $^{-1}$) which we associate with galaxy dynamics and merger remnants. Broad [O III] emission lines (FWHM ≈ 700 – 1400 km s $^{-1}$) are offset from these galaxy kinematics which we interpret as energetic outflows. The error bars indicate are representative 1σ uncertainties for the [O III] measurements. The horizontal solid lines indicate the approximate uncertainties in the spatial positions of the measurements when applicable. The dotted lines indicate zero velocity using the redshift of the narrowest [O III] components in the galaxy-integrated spectra (Fig. 3).

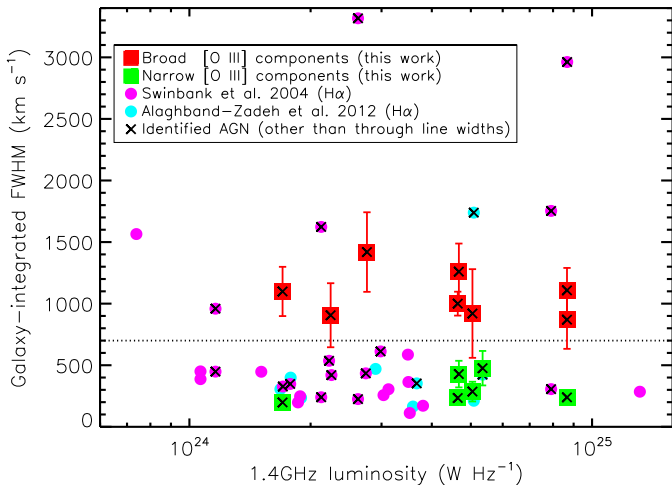


Figure 7. The [O III] FWHM from the galaxy-integrated spectra of our eight [O III] detected targets and high-redshift ULIRGs from the literature versus 1.4 GHz radio luminosity. Both broad components ($\text{FWHM} \geq 700 \text{ km s}^{-1}$; dashed line) and narrow components of the profile fits have been plotted (see Table 3). For SMMJ0217–0503 we have plotted the northern and southern systems separately (see Table 4). We also plot the galaxy integrated $\text{H}\alpha$ FWHMs from other high-redshift ULIRGs with similar radio luminosities (Swinbank et al. 2004; Alaghband-Zadeh et al. 2012). The sources that are identified as AGN (using methods not based on emission-line widths), have been highlighted (see § 5.1 for details). The non-AGN ULIRGs have FWHMs that lie below $\approx 700 \text{ km s}^{-1}$. The narrow [O III] components of our sample are consistent with the emission-line widths from non-AGN ULIRGs and presumably trace galaxy dynamics and mergers while the broadest components appear to be constrained to the AGN host galaxies and are likely to be tracing AGN-driven outflows.

is observed. For SMM 1636+4057 we use half of the velocity offset between the two broad components, which is also consistent with the offset between each component and the velocity of the $\text{H}\alpha$ broad-line region (see Appendix A8).

5 DISCUSSION

Our IFU observations of eight $z = 1.4 - 3.4$ ULIRGs that host AGN activity have revealed extreme gas kinematics with very broad [O III] emission ($\text{FWHM} \approx 700 - 1400 \text{ km s}^{-1}$), extended up to 15 kpc and with high-velocity offsets, up to $\approx 850 \text{ km s}^{-1}$. We have also identified narrow [O III] emission lines with moderate widths and velocity gradients ($\text{FWHM} \lesssim 500 \text{ km s}^{-1}$; $\Delta v \lesssim 200 \text{ km s}^{-1}$) over the full extent of the observed emission-line regions (up to ≈ 20 kpc). In the following discussion, we focus on the six sources for which we have high-quality spatially-resolved data and show that the narrow emission lines are consistent with tracing galaxy-dynamics and mergers, while the broadest emission lines are consistent with being predominantly due to energetic outflows. We then go on to discuss the impact that these outflows could be having on the future growth of the central BHs and host galaxies and the implications of these results for the formation of massive galaxies.

5.1 Tracing galaxy dynamics, mergers and outflows

In six of our sources we find an extended [O III] emission-line region (up to ≈ 20 kpc; Fig. 4), which are often found in

gas-rich systems containing luminous AGN (e.g., Colina et al. 1999; Nesvadba et al. 2008; Greene et al. 2011; Villar-Martín et al. 2011a; Matsuoka 2012). The presence of these emission-line regions enables us to trace the kinematics of the ionised gas in these galaxies.

We identified narrow [O III] emission (FWHM up to a few $\times 100 \text{ km s}^{-1}$) with irregular velocity profiles and small velocity gradients ($\Delta v \lesssim 200 \text{ km s}^{-1}$) over the full extent of the emission-line regions (Fig. 4 and Fig. 6). The line widths and velocity offsets observed in this narrow [O III] emission are similar to the kinematics of gas found in simulated merger remnants (Cox et al. 2006). The kinematics of these narrow emission lines are also broadly consistent with other high-redshift star-forming galaxies that have similar radio-luminosities, many of which are also undergoing mergers (e.g., Swinbank et al. 2004; Nesvadba et al. 2007b; Lehnert et al. 2009; Alaghband-Zadeh et al. 2012) as well as nearby ULIRGs (e.g., Colina et al. 2005). To illustrate this, in Fig. 7, we compare the galaxy-integrated emission-line FWHMs of our AGN sample to the $\text{H}\alpha$ emission line FWHM in other high-redshift ULIRGs from Swinbank et al. (2004) and Alaghband-Zadeh et al. (2012). We highlight sources that are identified as AGN on the basis of their emission-line ratios, X-ray emission, UV spectral features or their mid-infrared spectra. Fig. 7 shows that the narrow [O III] emission lines ($\text{FWHM} \lesssim 500 \text{ km s}^{-1}$) in our sources are comparable to the emission-line widths of non-AGN high-redshift ULIRGs and therefore are likely to be tracing the same kinematic components seen in these sources (i.e., galaxy dynamics and mergers). The velocity structure of the emission lines seen in the IFU data of the non-AGN ULIRGs (Alaghband-Zadeh et al. 2012) are also similar to the narrow [O III] components observed here. In particular, for the two sources where there are IFU observations covering both the [O III] and $\text{H}\alpha$ emission lines (SMMJ0217-0503 and RGJ0332-2732; this work and Alaghband-Zadeh et al. 2012) the kinematics of the narrow [O III] and $\text{H}\alpha$ emission-line components are roughly consistent (e.g., see Fig. 5).

In contrast to the narrow emission lines, the identification of broad emission lines ($\text{FWHM} \geq 700 \text{ km s}^{-1}$) in the galaxy integrated spectra of high-redshift ULIRGs appears to be constrained to galaxies that contain known AGN activity (Fig. 7).³ This is in agreement with studies of low-redshift ULIRGs where the broadest emission lines are found in systems hosting powerful AGN activity (e.g., Veilleux et al. 1999, Zheng et al. 2002; Westmoquette et al. 2012). Although broad emission-line components may be found in non-AGN high-redshift star-forming galaxies, they are generally faint and are difficult to identify other than by stacking the spectra of multiple sources or with excellent quality data (e.g., Swinbank et al. 2004; Nesvadba et al. 2007b; Le Tiran et al. 2011). However, we note that we are basing these arguments on small samples of galaxies which are biased in their selection and to fully address if bright and broad emission lines, such as those in our sources, are unique to galaxies hosting AGN activity, requires larger systematic samples of spectra and IFU data. In addition to comparisons with the literature, there is further evidence that the broadest emission lines are associated with AGN activity in our sample. The broadest emission lines are found to be spatially co-

³ The one source from Swinbank et al. (2004) with $\text{FWHM} > 700 \text{ km s}^{-1}$ that is not identified as an AGN (Fig. 7) has a complex spectrum and has not been covered by multi-wavelength observations in the literature. It is therefore not possible to rule out the presence of a significant AGN in this galaxy.

incident with the most likely location of the AGN in these galaxies based on very high [O III]/H β emission-line ratios (see §4.3). The most striking example of this is the source SMMJ1636+4057 where the broadest [O III] emission lines are found to be co-spatial with the AGN, and not in the region of unobscured star formation (details in Appendix A8).

Broad and asymmetric [O III] $\lambda\lambda$ 4959,5007 emission-line profiles, such as those found in this work, are most commonly attributed to high-velocity outflowing gas (e.g., Heckman et al. 1981; Greene & Ho 2005; Barth et al. 2008; Nesvadba et al. 2008; Greene et al. 2011). In particular IFU observations of local ULIRGs that host AGN activity reveal broad and spatially extended emission lines (similar to those that we observe) associated with energetic outflows (Rupke & Veilleux 2011; Westmoquette et al. 2012). On the basis of the above arguments the broadest kinematic components (FWHM \gtrsim 700 km s $^{-1}$) appear to be associated with AGN activity and therefore do not appear to be the result of mergers and galaxy dynamics or even (as we will further argue below) star-formation driven outflows, and therefore AGN-driven outflows is the most natural explanation. We find convincing evidence for extended (\gtrsim 4 kpc) outflows in four of our sample (RG J0302+0010; SMMJ0943+4700; SMMJ1237+6203 and SMMJ1636+4057). The source RG J0332-2732 only has very broad [O III] emission lines in the most central regions, and the broad [O III] emission line in the source SMMJ0217-0503 has a low signal-to-noise ratio and is spatially unresolved. These two sources have lower quality data than the other four spatially extended sources and the evidence for outflows in these objects is weaker (see Appendix A1 and A4 for further discussion on these two sources).

5.2 Outflow properties

We can use the measured properties of the broad [O III] emission to place constraints on the outflow properties. In Fig. 8 we plot the observed spatial extent of the broad [O III] emission lines against the velocity offset from the systemic redshifts of the host galaxies (values are from the fits to the spectra shown in Fig. 5 and are provided in Table 4).⁴ The dashed lines in Fig. 8 represent estimated energy injection rates which we discuss later. The broad [O III] emission-line properties ($\Delta v \approx 50$ –850 km s $^{-1}$; spatial extent ≈ 4 –15 kpc) can be explained by the presence of an AGN-driven bi-polar outflow plus the addition of obscuring material in the host galaxy. In Fig. 9 we show a simple schematic diagram to attempt to explain the properties and diversity of the broad [O III] emission lines. Hydrodynamical simulations and analytical models predict that a powerful AGN-wind, launched from the central BH, could sweep up clouds of gas resulting in an kpc-scale outflow (e.g., Debuhr et al. 2012; Zubovas & King 2012 and references therein). Galaxy-wide outflows are thought to be expanding bubbles on either side of the host galaxy, being forced into this shape by the denser material in the centre of the host-galaxy (e.g., Zubovas & King 2012; Faucher-Giguere & Quataert 2012). As we are observing the outflow through luminous [O III] emission, the *observed* properties of the outflow will also depend on the size and orientation of the AGN ionisation cones (e.g., Crenshaw et al. 2010). Multiple clouds being

caught up in the bulk flow of the outflow (e.g., Zubovas & King 2012) or perturbed ionised gas would result in broad [O III] emission lines (e.g., Villar-Martín et al. 2011b). The ‘near-side’ of the outflow would therefore be observed as a broad and blueshifted emission line and the ‘far-side’ would be observed as broad and redshifted emission (see Fig. 9). However, part of the outflow could be obscured by material in the host galaxy, as is likely to be the case in clumpy and dusty systems such as high-redshift ULIRGs (e.g., Ivison et al. 2007; Tacconi et al. 2008; Engel et al. 2010). High-redshift ULIRGs are kinematically disturbed, potentially resulting in a complex distribution of obscuring material, which, along with the relative orientation of the AGN, could explain why in some cases we only see either a blueshifted (i.e., when only the near-side of the outflow is observed) or redshifted broad emission line (i.e., when only the far-side of the outflow is observed; also see Fig. 6 and 7 in Crenshaw et al. 2010).

The range in spatial extents and velocity offsets of the implied outflows that we observe (Fig. 8) can also be explained using this simple model (Fig. 9). The *observed* velocity offsets and *observed* spatial extents will be highly dependent on the orientation of the outflow with respect to the line of sight. If the axis of the outflow is orientated along the line of sight, high velocity offsets and a small spatial extent would be observed (e.g., this could explain the properties of SMMJ1636+4057). Conversely, if the axis of the outflow is in the plane of the sky, a small velocity offset and a large spatial extent would be observed (e.g., this could explain the properties of SMMJ0943+4700); see Appendix A for further discussion on individual sources. In contrast, the observed FWHM will be less dependent on the orientation. We emphasise that this is a very simplified model and other interpretations could also be valid. For example, the observed emission-line properties will also be dependent on the intrinsic properties of the outflow, such as their intrinsic velocity and distance traveled from the BH.

We have argued that the measured velocity offsets observed may not represent the true velocity of the outflow due to an orientation effect. We attempt to estimate corrected velocity offsets by taking the two sources which contain a known broad-line AGN (SMMJ1237+6203 and SMMJ1636+4057; see Appendix A for details). In these sources the identification of the broad-line AGN component suggests that the outflow could be primarily orientated towards us and therefore the observed velocity offset is likely to be close to the true outflow velocity. For these two sources we find that the average of FWHM/ Δv is ≈ 2 ; reassuringly we also find a median ratio of FWHM/ $\Delta v \approx 2$ for low-redshift broad-line AGN that display [O III] properties indicative of outflows (data from Mullaney et al. in prep). We therefore suggest that FWHM/2 may be an adequate approximation of the true outflow rate, although subject to large uncertainties. Using this as a diagnostic, we estimate bulk outflow velocities in the range of ≈ 300 –700 km s $^{-1}$, which are similar to the predicted kpc-scale outflow velocities predicted by hydrodynamical simulations and analytical models of outflows (≈ 300 –1500 km s $^{-1}$), driven by AGN in objects with similar properties to the sources in our sample (i.e., ULIRGs, with $L_{\text{AGN}} \approx 10^{46}$ erg s $^{-1}$; Debuhr et al. 2012; Zubovas & King 2012; Faucher-Giguere & Quataert 2012).

5.2.1 Estimating outflow energy rates and determining what is powering the outflows

To attempt to quantify the impact the outflows may be having on the host galaxies we consider approaches to estimate the energy injection rates into the ISM. We do not have good constraints on

⁴ The source SMMJ1237+6203 does not appear in this table. For this source we use a spatial extent of 5 kpc (see Fig. 6) and the FWHM and velocity offset from the galaxy-integrated spectrum (Table 3). See the end of §4.4 for details.

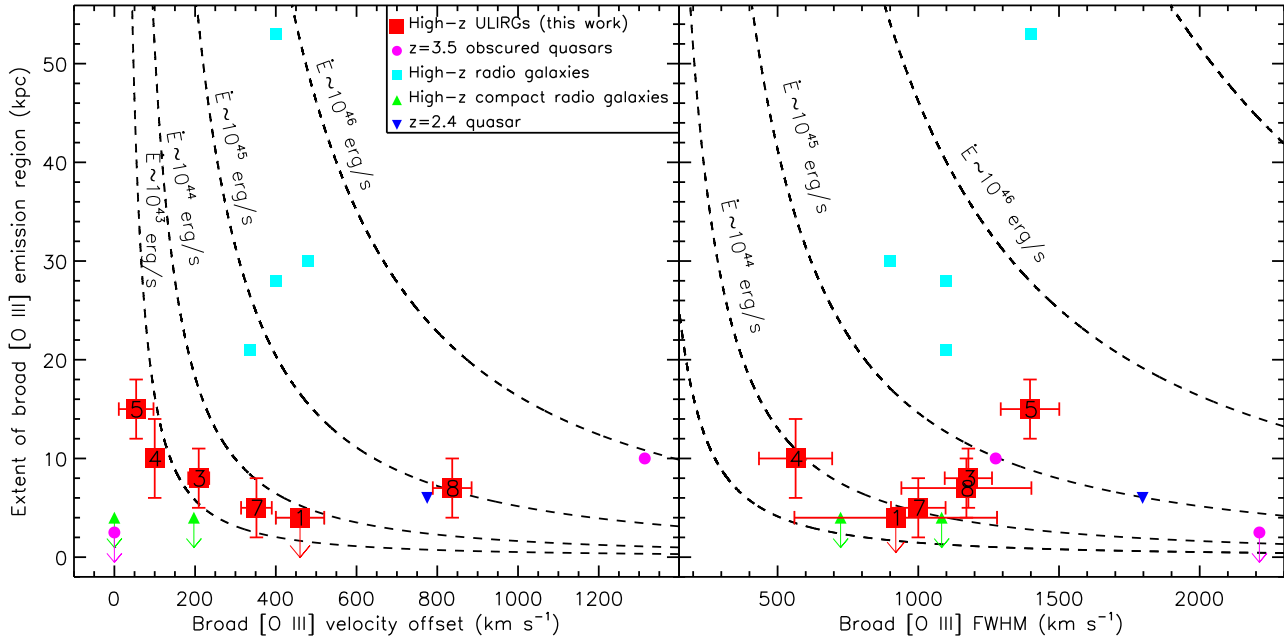


Figure 8. The projected spatial-extent of the broad [O III] emission-line regions against velocity offset from the systemic redshift (*left*) and FWHM (*right*) for our spatially resolved sources (see Table 3 and Table 4). The numbers inside the symbols correspond to the source IDs. Also shown are other high-redshift sources with IFU data (symbols are the same as in Fig. 1). If two sides of an outflow are observed, half of the velocity difference between them is used, and the average FWHM of each side. For spatially unresolved data we use the seeing disk as an upper limit of the extent. For illustrative purposes, the dashed lines show the expected energy injection rates (\dot{E}) using a simple outflow model (see §5.2 for details). Strong evidence for extended outflows is not confirmed for source IDs 1 and 4 (see §5.1). Despite 3–4 magnitudes difference in radio luminosities, HzRGs and high-redshift ULIRGs containing AGN activity have comparable velocity offsets and emission-line widths and are both potentially dumping energy into their host galaxies at considerable rates ($\approx 10^{43}$ – 10^{46} erg s $^{-1}$).

mass of the gas entrained in the outflows or on the geometry of the outflow, making such estimates uncertain. For illustrative purposes, we consider the energy injection rates assuming an energy conserving bubble into a uniform medium (e.g., Heckman et al. 1990; Veilleux et al. 2005; Nesvadba et al. 2008; and references therein) which gives the following relation:

$$\dot{E} \approx 1.5 \times 10^{46} r_{10}^2 v_{1000}^3 n_{0.5} \text{ erg s}^{-1}, \quad (1)$$

where r_{10} is taken to be half the extent of the observed broad [O III] emission (in units of 10 kpc) and v_{1000} are the velocity offsets in units of 1000 km s $^{-1}$ (see Table 4). The ambient density (ahead of the expanding bubble), $n_{0.5}$, is in units of 0.5 cm $^{-3}$ for which we have assumed $n_{0.5}=1$.⁵

In the left panel of Fig. 8 we plot on tracks indicating fixed energy injection rates using Equation 1. We have already dis-

cussed that the observed velocity offsets are unlikely to be representative of the intrinsic velocities and that FWHM/2 is plausibly a better estimate of the true outflow velocity. Therefore, in the right panel of Fig. 8 we plot the extent of the broad [O III] emission against FWHM and tracks of constant energy injection rates using Equation 1, but replacing the velocity offset with FWHM/2. For the two sources with a known broad-line AGN in this sample (SMM J1237+6203 and SMM J1636+4057) and the sources with broad-line AGN in the comparison samples (i.e. Nesvadba et al. 2006; Cano-Díaz et al. 2012), the two diagnostics for the bulk outflow velocity give energy injection rates that are consistent within a factor of a few. We establish that the spatially extended outflows in these high-redshift ULIRGs are potentially injecting energy into their host galaxies at considerable rates of $\approx (0.08\text{--}3) \times 10^{45}$ erg s $^{-1}$, where the range indicates the values for different sources. Over a typical AGN lifetime of 30 Myr (e.g., Hopkins et al. 2005) the total energy injection would be of order $\approx (0.8\text{--}28) \times 10^{59}$ ergs; however, we note that outflows could continue ~ 10 times longer than the active time of the BH (King et al. 2011) which would increase this energy injection by another order of magnitude. These outflow energy injection rates are comparable to the typical binding energy of the host galaxies in these systems of $\approx 10^{59}$ ergs (assuming a spheroid mass of $\approx 10^{11} M_{\odot}$, a velocity dispersion $\sigma \approx 200$ km s $^{-1}$ and $R_e=4$ kpc; e.g., Binney & Tremaine 1987) and demonstrate that these outflows could unbind at least a fraction of the ISM from the host galaxies.

We next consider what could be powering the outflows based on energetic arguments. In Fig. 10 we compare the ratio of the outflow energy rates with the potential energy input rates from: (1) the radiative output of the AGN (i.e. the AGN bolometric luminos-

⁵ This density assumption is based on the the values of $n_{0.5}=1\text{--}4$ used in e.g. Heckman et al. (1990) and Nesvadba et al. (2008). This value can be indirectly estimated from the (post-shock) electron density (see Heckman et al. 1990 and references therein for further details), derived from the [S II] $\lambda\lambda 6171, 6731$ emission-line doublet which is sensitive to electron densities in the range 100– 10^5 cm $^{-3}$ (Osterbrock 1989). We used a stack of the rest-frame optical spectra of the high-redshift ULIRGs from Swinbank et al. (2004) to derive a flux ratio of $R_{[\text{SII}]} = F_{\lambda 6716}/F_{\lambda 6731} = 1.1 \pm 0.3$. This is consistent with the HzRGs of Nesvadba et al. 2008 who find $R_{[\text{SII}]}=1.0\text{--}1.1$, such that the implied densities of HzRGs and high-redshift ULIRGs are similar. We therefore use the same value of $n_{0.5} = 1$ as in Nesvadba et al. (2008). Although we have no direct way of measuring $n_{0.5}$ this unknown will only vary our order-of-magnitude estimates of the energy injection rates by a factor of a few.

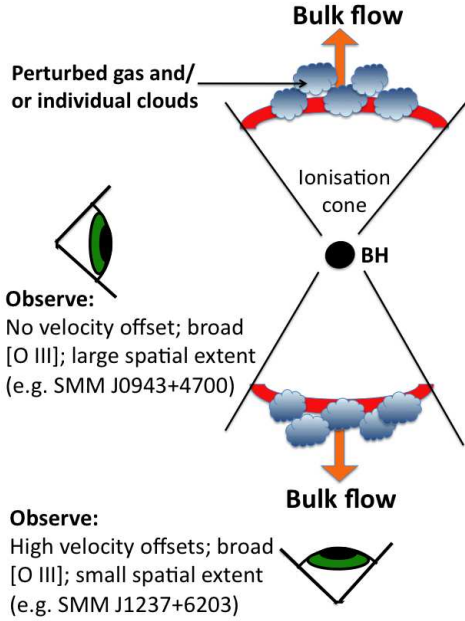


Figure 9. A schematic diagram to illustrate a possible interpretation of the observations of the broad [O III] emission lines. If a fast wind is initially launched around the central BH it could sweep up clouds of gas in a bi-polar outflow (as assumed by some models e.g., Debuhr et al. 2012; Zubovas & King 2012; see § 5.2 for more discussion). The orientation with respect to the line of sight will determine the velocity offsets and spatial extent observed; however, broad emission lines will be always be observed. This could explain the diversity in the properties of our observations. In addition, obscuring material in the host galaxy would result in parts of the outflow not being visible which could explain why in some sources we only observe either blueshifted or redshifted broad emission lines.

ity; L_{AGN}) and (2) energy output from star formation (\dot{E}_{SF}). We calculate outflow energy injection rates using Equation 1, replacing v with $\text{FWHM}/2$ and r as half the spatial extent of the broad [O III] region (see Table 4; also see footnote 4). We have estimated the bolometric luminosity of the AGN using SED modeling (described in §3; values given in Table 2). We estimate the potential energy input from star-formation using the star formation rates from our SED modelling (Table 2) and assuming that the mechanical energy injection from supernovae and stellar winds would be at most $\approx 7 \times 10^{41} (\text{SFR}/M_{\odot} \text{ yr}^{-1}) \text{ erg s}^{-1}$ (following Leitherer et al. 1999 and Veilleux et al. 2005).⁶ We note that the assumptions made are highly idealistic, and we have not, for example, considered the case of a momentum conserving outflow. However, Nesvadba et al. (2006, 2008) follow several methods to estimate the energy injection in similar outflows in HzRGs and find that the different methods generally agree on the order of magnitude level (also see Veilleux et al. 2005 for further discussion on the energetics of outflows and the potential energy input from star formation and AGN activity).

Fig. 10 demonstrates that the radiative output of the AGN is energetically viable as the dominant power source of the outflows

⁶ If we were to follow instead Dalla Vecchia & Schaye (2008) to estimate this energy input, the values would be a factor of ≈ 2 lower. Conversely, radiation pressure from star-formation could potentially contribute a comparable amount of pressure to stellar and supernovae winds in ULIRGs (Veilleux et al. 2005). As we are considering order of magnitude estimates only, these uncertainties do not affect our conclusions.

observed in all of these sources. Assuming the bolometric luminosity provides an estimate of the initial energy input from the AGN, so long as ≈ 0.2 – 5% of this energy can couple to the ISM, the radiative power of the AGN in these systems is large enough to drive the observed outflows. This range of coupling efficiencies is similar to the values required by many models to reproduce the properties of local massive galaxies (e.g., Springel et al. 2005; Di Matteo et al. 2005; Debuhr et al. 2012). In contrast, the required coupling efficiencies for star formation are an order of magnitude higher ($\approx 15\%$ to $\gg 100\%$). For the three sources with implied coupling efficiencies of ≈ 15 – 50% star formation may play a significant role; however, based on the observed properties of the broad [O III] emission presented earlier (see §5.1), and the energetic arguments presented here, we tentatively suggest that the AGN may play a dominant role in powering the outflows. Given the current quality of the available data, a more detailed analysis is not yet warranted and the values of input energetics should be used with care.

5.2.2 The potential fate of the outflowing gas

Based on energetic arguments we have already demonstrated that the outflows we observe are likely to unbind the gas from the host galaxies. However, many models of galaxy formation require powerful AGN-driven outflows to remove the gas completely from the host galaxy potentials to efficiently truncate star formation and remove the fuel for future accretion onto the BHs (e.g., Di Matteo et al. 2005; Hopkins et al. 2008). Will the outflowing gas we observe be able to escape the host galaxy and consequently remove the gas supply for further star formation and future accretion? In Fig. 10 we plot the broad [O III] velocity offset against FWHM for our spatially resolved sources and also plot other high-redshift AGN with available IFU data from the literature. By taking an estimated galaxy mass of $10^{11} M_{\odot}$ (typical of these sources; e.g., Engel et al. 2010; Wardlow et al. 2011; Hainline et al. 2011) the escape velocity at a distance of 4 kpc would be $v_{\text{esc}} \approx 460 \text{ km s}^{-1}$ (see Fig. 10). Considering the observed velocity offsets ($\Delta v = 50$ – 850 km s^{-1}), only the outflows in two sources (SMM J1636+4057 and SMM J0217–0503) appear likely to exceed this escape velocity. However, if we instead consider the the *maximum* velocities of the emission-line gas ($v_{\text{max}} \approx 400$ – 1400 km s^{-1} ; defined as $v_{\text{max}} = |v| + \text{FWHM}/2$; i.e., Rupke et al. 2005a,b) then the outflow velocities are found to exceed the escape velocity (see dashed curve in Fig. 10) in all sources except RG J0332–2732, suggesting that some fraction of the gas is able to escape the host galaxy potential.

Unless the gas is completely removed from the host galaxy potential, or is unable to cool on short timescales, significant star formation and BH accretion may be able to recommence after the outflow episode. We therefore consider a simplified approach to investigate if the outflowing gas will be able to escape the dark-matter halo. Assuming a static dark matter halo with a mass of $\approx 10^{13} M_{\odot}$ (expected for these sources; Hickox et al. 2012), a Navarro Frenk and White (NFW; Navarro et al. 1996) density profile, and a point mass of $\approx 10^{11} M_{\odot}$ (i.e., the host galaxy), a particle initially at $\approx 4 \text{ kpc}$ from the centre of the host galaxy would need to be travelling at $v \approx 1000 \text{ km s}^{-1}$ to escape beyond the virial radius of the halo ($\approx 440 \text{ kpc}$; M. Lovell priv. comm.; see Fig. 10). On the basis of this simple model, where we assume the effects of gravity only, particles travelling at ≈ 400 – 800 km s^{-1} at $\approx 4 \text{ kpc}$ will return to the host galaxy within a few hundred Myrs. From this analysis only two sources have maximum outflow velocities that could potentially unbind some fraction of the gas from the dark matter halo (Fig. 10), which suggests that the gas in the majority of

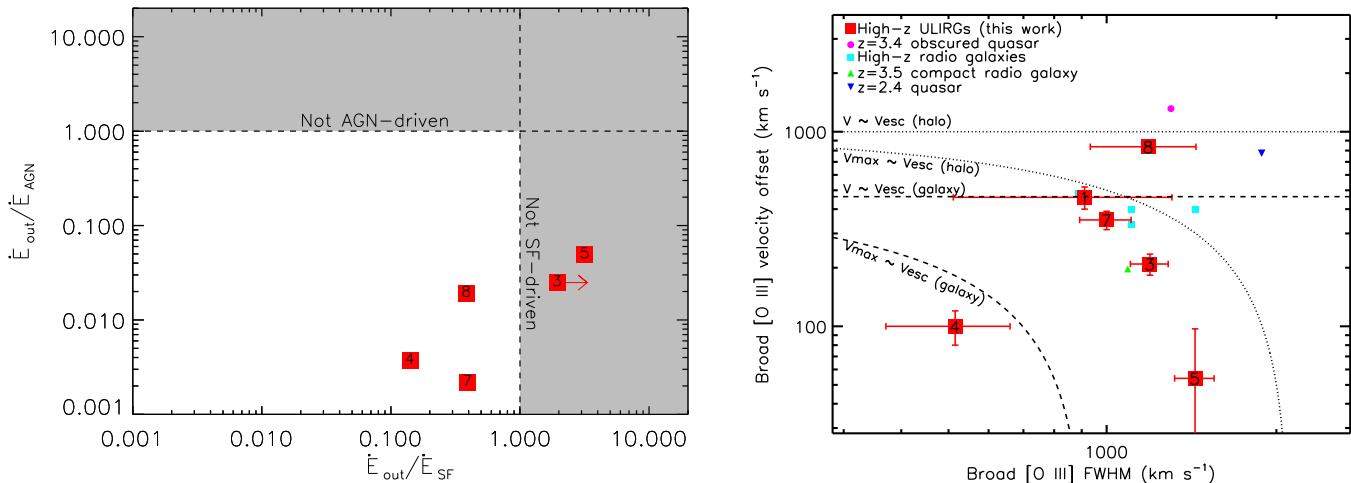


Figure 10. *Left:* The ratio of the estimated outflow energy rate (\dot{E}_{out}) to the derived input energy rate from AGN (\dot{E}_{AGN}) against the ratio of the outflow energy rate to the predicted energy input rate from star formation (\dot{E}_{SF}) for five of the six sources with spatially resolved [O III] emission. For the sixth source we only have upper limits for both \dot{E}_{AGN} and \dot{E}_{out} and therefore have no constraints on the ratio of these quantities. The numbers inside the symbols correspond to the source IDs. We note that we lack strong evidence for extended outflows for source IDs 1 and 4 (see §5.1.) The shaded regions indicate where a $>100\%$ coupling efficiency is required between the input energy and the gas to power the outflows, effectively ruling out such an input energy mechanism. The bolometric luminosity of the AGN appears to be energetically favourable to power all the outflows requiring only $\approx 0.2\text{--}5\%$ of the bolometric output to couple to the gas; however star formation cannot be ruled out in all cases. It should be noted that the values used rely heavily on assumptions and should be taken as illustrative only, with uncertainties at the order of magnitude level. Details of the derived values that are plotted are provided in §5.2 (also see Table 2). *Right:* Broad [O III] emission-line velocity offset versus FWHM for the spatially resolved sources in our sample (values taken from regions of broad [O III]; see Table 4). Also shown are other high-redshift sources with IFU data as described in Fig. 1. The maximum velocities ($v_{\text{max}} = |v| + \frac{1}{2}\text{FWHM}$) of the gas are potentially high enough to exceed the typical escape velocity of a typical massive galaxy ($10^{11} M_{\odot}$ at 4 kpc; dashed curve). However, using simplistic arguments (see §5.2) only one of our sources has a maximum outflow velocity that could potentially unbind some of the gas from a typical galaxy halo ($\approx 10^{13} M_{\odot}$ at ≈ 4 kpc; dotted curve).

the systems may eventually cool and re-ignite another episode of AGN activity and star formation. However, it has been proposed that *quasar mode* outflows, such as those observed here, may be an effective way of “pre-heating” the gas at early times prior to a mechanical-heating dominated phase (i.e., the so-called *radio mode*), which will then efficiently prevent the gas from cooling (e.g., van de Voort et al. 2011; McCarthy et al. 2011). The outflows we observe could be a means of energetically pre-heating and ejecting gas at high redshift and therefore could be a crucial stage in the evolution of massive galaxies. In this scenario these galaxies will therefore be the progenitors of the radiatively weak, low-redshift AGN in massive galaxies which are observed to have mechanical heating that is preventing gas from cooling (Best et al. 2005, 2006; Smolčić et al. 2009; Danielson et al. 2012).

6 CONCLUSIONS

We have taken Gemini North-NIFS and VLT SINFONI IFU observations around the emission-line doublet [O III] $\lambda\lambda 4959, 5007$ of eight high-redshift ULIRGs that host AGN activity. Our aim was to search for broad, high-velocity and spatially extended [O III] emission as a tracer of powerful AGN-driven outflows over galaxy-wide scales that are predicted by the *quasar-mode* in galaxy evolution models. We have strong evidence that such outflows exist in at least a fraction of the high-redshift ULIRGs. Our main conclusions are the following:

(i) We find narrow [O III] emission lines (FWHM \approx few hundred km s^{-1}) extended over galaxy-wide scales (up to ≈ 20 kpc).

By comparing these observations with high-redshift ULIRGs that are also undergoing intense starbursts and mergers but do not host significant AGN activity we show that the narrow [O III] emission lines we observe (FWHM up to a few 100 km s^{-1}) are consistent with tracing host galaxy dynamics and merger remnants (§5.1).

(ii) In the four most luminous sources we find extremely broad [O III] $\lambda\lambda 4959, 5007$ emission (FWHM $\approx 700\text{--}1400 \text{ km s}^{-1}$) with high velocity-offsets (up to $\approx 850 \text{ km s}^{-1}$), extended over $\approx 4\text{--}15$ kpc; i.e., the key signatures of galaxy-scale energetic outflows (§5.1). The other four sources exhibit broad [O III] emission but we have limited constraints on the spatial extent of the broad [O III] emission due to lower quality data.

(iii) We apply a simple outflow model to show that the spatially extended outflows are potentially moving through the ISM with an energy rate of $\approx (0.08\text{--}3) \times 10^{45} \text{ erg s}^{-1}$, sufficient to unbind some of the gas from the host galaxy and potentially disrupting future accretion and star-formation in the host galaxy (§5.2.1). These order of magnitude estimates are model dependent and rely on estimates of the density and therefore should be considered as illustrative only.

(iv) By estimating the energy injection rates from the AGN and star formation driven winds we find that the outflows require $\approx 0.2\text{--}5\%$ of the AGN luminosity to couple to the gas, while star formation require coupling efficiencies of $15\%\text{--}\gg 100\%$ (§5.2.1). We use a combination of energetic arguments and comparison to non-AGN systems to show that, although star formation may also play a significant role in some sources, the AGN activity is feasibly the dominant power source for driving the outflows in all sources.

(v) The high maximum outflow velocities observed in these

galaxies suggest that at least some fraction of the gas will be unbound from the host galaxies, but significant fractions of gas are very unlikely to be completely unbound from the galaxy haloes (§5.2.2).

The galaxies observed here are two to three orders of magnitude more common than the extreme high-redshift radio galaxies that are often associated with powerful AGN large-scale outflows at high redshift. We have shown that energetic large-scale outflows are present in at least a fraction of high-redshift ULIRGs that host AGN activity, which are believed to be the progenitors of today's massive elliptical galaxies. We have suggested that these outflows may be a crucial phase in the evolution of massive galaxies.

Acknowledgments

We gratefully acknowledge support from the Science and Technology Facilities Council (CMH; DMA; AMS; SA-Z; ADM). IRS acknowledges a Leverhulme Senior Fellowship. FEB acknowledges support from Basel-CATA (PFB-06/2007) and CONICYT-Chile (FONDECYT 1101024). We thank Mark Lovell for useful discussions, Ric Davies for providing his sky-subtraction code. We thank the referee for detailed comments. This work is based on observations carried out with the Very Large Telescope of ESO (Programme ID: 087.A-0660(A)) and on observations obtained at the Gemini Observatory (Programme IDs: GN-2008A-Q-58 and GN-2009B-Q-1), which is operated by the Association of Universities for Research in Astronomy, Inc., under a cooperative agreement with the NSF on behalf of the Gemini partnership: the National Science Foundation (United States), the Particle Physics and Astronomy Research Council (United Kingdom), the National Research Council (Canada), CONICYT (Chile), the Australian Research Council (Australia), CNPq (Brazil) and CONICET (Argentina). This publication makes use of data products from the *Wide-field Infrared Survey Explorer*, which is a joint project of the University of California, Los Angeles, and the Jet Propulsion Laboratory/California Institute of Technology, funded by the National Aeronautics and Space Administration. This research has made use of data from HerMES project (<http://hermes.sussex.ac.uk/>). HerMES is a *Herschel* Key Programme utilising Guaranteed Time from the SPIRE instrument team, ESAC scientists and a mission scientist. HerMES will be described in Oliver et al. 2012, MNRAS. *Herschel* is an ESA space observatory with science instruments provided by European-led Principal Investigator consortia and with important participation from NASA.

TARGET SED DATA AND DERIVED PROPERTIES

ID	Source	S_8	S_{24}	S_{70}	S_{250}	S_{350}	S_{500}	S_{850}	$L_{\text{IR,SF}}$	SFR	$L_{\text{AGN,SED}}$
(1)	(2)	(μJy)	(mJy)	(mJy)	(mJy)	(mJy)	(mJy)	(mJy)	($10^{12}L_{\odot}$)	($M_{\odot}\text{yr}^{-1}$)	(10^{46}erg s^{-1})
		(3)	(4)	(5)	(6)	(7)	(8)	(9)	(10)	(11)	(12)
1	SMMJ0217–0503	44.7±2.3	0.49±0.05	-	36.3±5.8	33.9±6.3	21.7±6.8	4.4±1.7	4.5±0.8	780±160	<0.2
2	SMMJ0302+0006	63.4±6.8	0.45±0.05	<13.6	-	-	-	4.4±1.3	2.0±0.3	340±50	0.14±0.09
3	RGJ0302+0010	-	<0.24	-	-	-	-	<4.5	<2.1‡	<360	2.0±0.2**
4	RGJ0332–2732	7.8±0.2	0.94±0.09	-	27.5±5.8	27.5±6.3	20.3±6.8	<3.6	4.9±0.9	850±120	2.2±0.4
5	SMMJ0943+4700*	-	0.57±0.06	-	22.6±5.8	26.5±6.3	17.3±6.8	8.7±1.5	7.5±1.5	1300±200	5.8±0.2
6	SMMJ1235+6215	64.1±22	0.63±0.06	<4.1	30.4±5.8	37.4±6.3	27.0±6.8	8.3±2.5	6.9±1.0	1200±170	0.7±0.4
7	SMMJ1237+6203	(1.02±0.09)†	(1.61±0.7)†	<6.0	<14	<24	<24	5.3±1.7	2.4±0.2	430±50	5.33±0.05
8	SMMJ1636+4057	66.8±6.8	0.95±0.1	<9.1	44.4±5.8	36.6±6.3	29.0±6.8	8.2±1.7	7.9±1.5	1400±200	1.9±0.6

Table 2. NOTES:

Column (1): Source ID. Column (2): Source name. Column (3): $8\mu\text{m}$ flux densities and their uncertainties taken from: Hainline et al. (2009); Cardamone et al. (2010); or the Spitzer archive. Column (4): $24\mu\text{m}$ flux densities from: Ivison et al. (2007); Valiante et al. (2007); Menéndez-Delmestre et al. (2009); Dickinson et al. in prep; or the Spitzer archive. Uncertainties are assumed to be 10% of the measured values. Column (5): $70\mu\text{m}$ flux densities taken from Hainline et al. (2009). Columns (6)–(8): The $350\mu\text{m}$, $450\mu\text{m}$ and $500\mu\text{m}$ flux densities. This HerMES data was accessed through the HeDaM database (<http://hedam.oamp.fr>) operated by CeSAM and hosted by the Laboratoire d’Astrophysique de Marseille. The uncertainties quoted are the confusion noise for each band. Column (9): $850\mu\text{m}$ flux densities and their uncertainties taken from: Cowie et al. (2002); Chapman et al. (2004); Chapman et al. (2005); Clements et al. (2008). Column (10): Derived IR luminosities ($8\text{--}1000\mu\text{m}$) from the star formation component of the SED fitting procedures described in §3. Column (11): Star formation rates derived using the quoted $L_{\text{IR,SF}}$ values and the relationship from Kennicutt (1998). Column (12): The estimated AGN bolometric luminosity calculated using the methods outlined in §3. ‡The value quoted is calculated using the radio-infrared correlation (assuming a $q = 2.1$). This is an upper limit as there will be an unknown AGN contribution to the radio flux. **This AGN bolometric luminosity is derived from the [O III] luminosity (see §3). * For SMMJ0943+4700 the flux densities have been corrected for an amplification factor of 1.2. We note that the quoted flux densities will cover both radio counterparts to this source (see Appendix A5). †These are the $12\mu\text{m}$ and $22\mu\text{m}$ flux densities taken from the *Wide-field Infrared Survey Explorer* archive.

 GALAXY-INTEGRATED [O III] λ 5007 EMISSION-LINE PROPERTIES

ID	Source	Component A.			Component B			Δv	Total [O III] Luminosity
		$z_{[\text{OIII}],A}$	FWHM _A	Flux _A	$z_{[\text{OIII}],B}$	FWHM _B	Flux _B		
(1)	(2)	(3)	(km s^{-1})	($10^{-16}\text{erg s}^{-1}\text{cm}^{-2}$)	(6)	(km s^{-1})	($10^{-16}\text{erg s}^{-1}\text{cm}^{-2}$)	(km s^{-1})	(10^{42}erg s^{-1})
		(3)	(4)	(5)	(6)	(7)	(8)	(9)	(10)
1	SMMJ0217–0503	2.0213[6]	540±170	3.1±0.7	-	-	-	-	9.3
2	SMMJ0302+0006	1.4049[10]	900±300	1.3±0.4	-	-	-	-	1.6
3	RGJ0302+0010	2.23861[12]	200±40	0.87±0.17	2.2419[7]	1100±120	2.7±0.4	+300±60	13.9
4	RGJ0332–2732	2.3145[5]	480±140	2.3±0.5	-	-	-	-	9.9
5	SMMJ0943+4700*	3.3506[4]	430±110	1.1±0.5	3.3503[8]	1300±200	2.6±0.4	+20±60	38.4
6	SMMJ1235+6215	2.199[2]	1500±500	1.2±0.4	-	-	-	-	4.5
7	SMMJ1237+6203	2.07502[3]	234±10	4.1±0.2	2.0714[4]	1000±100	2.9±0.3	–350±40	22.5
8	SMMJ1636+4057	2.38500[12]	240±30	1.3±0.3	2.3817[18]	900±200	1.0±0.4	–290±160	16.8
					2.4003[10]	1100±180	1.4±0.2	+1350±90	

Table 3. NOTES:

The properties of the galaxy-integrated [O III] emission-line profiles shown in Fig. 3. Numbers in square brackets give the uncertainty in the last decimal place. Column (1): Source ID. Column (2): Source name. Columns (3)–(5): Properties of the narrowest Gaussian components (Component A): redshift, FWHM and flux respectively. Columns (6)–(8): Same as the previous three columns but for the broader Gaussian components (Component B). Column (9): The velocity offset between the two Gaussian components. Column (10): The total [O III] luminosity. The bottom line of the table gives the properties of the third Gaussian component which is fit to the profile of SMMJ1636+4057. Flux and luminosity values are not extinction corrected. The quoted uncertainties are from the parameters of the emission-line fits. The true uncertainties on the fluxes are a factor or $\approx 2\text{--}3$ higher, due to uncertainties in the absolute flux calibration. *The flux values for SMMJ0943+4700 have been corrected for an amplification factor of 1.2.

ID (1)	Source (2)	Region (3)	[O III] Component A.			[O III] Component B			H β			log([O III]/H β) (14)	Linear extent (15)	
			$z_{\text{[O III]A}}$ (4)	FWHM _A (5)	Flux _A (6)	$z_{\text{[O III]B}}$ (7)	FWHM _B (8)	Flux _B (9)	Δv (10)	$z_{\text{H}\beta}$ (11)	FWHM _{Hβ} (12)			Flux _{Hβ} (13)
1	SMM J0217–0503	BR	2.0229[11]	900 \pm 400	0.42 \pm 0.15	-	-	-	-460 \pm 60 \dagger	-	-	<0.31	>0.13	11 \pm 4
		NR	2.0209[2]	290 \pm 80	1.26 \pm 0.19	-	-	-	-	-	-	<0.34	>0.57	
3	RG J0302+0010	BR	2.23873[7]	180 \pm 20	0.53 \pm 0.06	2.2410[3]	1180 \pm 80	2.59 \pm 0.16	+210 \pm 30	2.2441[11]	780 \pm 170	0.34 \pm 0.10	0.97 \pm 0.13	8 \pm 3
		NR	2.23864[12]	200 \pm 30	0.17 \pm 0.02	-	-	-	-	-	-	<0.03	>0.73	6 \pm 3
4	RG J0332–2732	BR	2.3143[4]	560 \pm 130	0.81 \pm 0.16	-	-	-	-100 \pm 20 \dagger	-	-	<0.20	>0.61	10 \pm 4
		NR	2.3147[4]	510 \pm 130	0.62 \pm 0.12	-	-	-	-	-	-	<0.19	>0.52	11 \pm 4
5	SMM J0943+4700*	BR	3.3511[4]	340 \pm 70	0.44 \pm 0.13	3.3503[5]	1400 \pm 100	2.41 \pm 0.17	-50 \pm 40	3.3500[7]	430 \pm 120	0.30 \pm 0.09	0.97 \pm 0.12	15 \pm 3
		NR	3.3493[2]	400 \pm 40	0.48 \pm 0.04	-	-	-	-	-	-	<0.07	>0.71	8 \pm 3
8	SMM J1636+4057	BR	2.3834[8]	1100 \pm 170	0.77 \pm 0.12	2.4023[7]	1220 \pm 160	1.07 \pm 0.14	+1670 \pm 100 \ddagger	-	-	<0.11	>1.2	7 \pm 3
		NR	2.38481[7]	257 \pm 14	1.25 \pm 0.06	-	-	-	-	-	-	<0.11	>1.1	20 \pm 3

Table 4. NOTES:

The properties of the [O III] and H β emission-line profiles extracted from the sub-regions shown in Fig. 5. Column (1): Source ID. Column (2): Source name. Column (3): The spatial region from which the spectra are extracted, either the broad region (BR) or narrow region (NR); see §4.3. Columns (4)–(6): Properties of the narrowest [O III] Gaussian components (Component A): redshift, FWHM (km s $^{-1}$) and flux (10^{-16} erg s $^{-1}$ cm $^{-2}$) respectively. Columns (7)–(9): Same as the previous three columns but for the broader [O III] Gaussian components (Component B). Column (10): The velocity offset (km s $^{-1}$) between the two Gaussian components. Columns (11)–(13): Properties of the H β emission lines: redshift, FWHM (km s $^{-1}$) and flux (10^{-16} erg s $^{-1}$ cm $^{-2}$) respectively. Column (14): The logarithm of the ratio of the total [O III] and H β fluxes. Column (15): The approximate linear-extent, along the most extended axis, of the defined regions (kpc). We take the size of seeing disks as the uncertainty on these measurements. All flux limits are 3σ upper limits, which are calculated using the noise of the line-free continuum and the FWHM of the [O III] emission line from the same region. Flux values are not corrected for dust extinction. The quoted uncertainties are from the parameters of the emission-line fits. The true uncertainties on the fluxes will be a factor or ≈ 2 – 3 higher, due to uncertainties in the absolute flux calibration. *The flux values for SMM J0943+4700 have been corrected for an amplification factor of 1.2. \dagger These are the velocity offsets to the H α emission in this region. \ddagger For analysis purposes we define the velocity offset as half of this value, see §4.4 and Appendix A8 for details.

REFERENCES

- Alaghband-Zadeh et al. S., 2012, ArXiv e-prints, 1205.5452
- Alatalo et al. K., 2011, ApJ, 735, 88
- Alexander D. M., Bauer F. E., Chapman S. C., Smail I., Blain A. W., Brandt W. N., Ivison R. J., 2005, ApJ, 632, 736
- Alexander D. M., Hickox R. C., 2011, ArXiv e-prints, 1112.1949
- Alexander D. M., Swinbank A. M., Smail I., McDermid R., Nesvadba N. P. H., 2010, MNRAS, 402, 2211
- Alexander et al. D. M., 2003, AJ, 125, 383
- Alexander et al. D. M., 2008, AJ, 135, 1968
- Barth A. J., Greene J. E., Ho L. C., 2008, AJ, 136, 1179
- Best P. N., Kaiser C. R., Heckman T. M., Kauffmann G., 2006, MNRAS, 368, L67
- Best P. N., Kauffmann G., Heckman T. M., Brinchmann J., Charlot S., Ivezić Ž., White S. D. M., 2005, MNRAS, 362, 25
- Binney J., Tremaine S., 1987, Galactic dynamics. Princeton series in astrophysics, Princeton University Press
- Blustin et al. A. J., 2003, A&A, 403, 481
- Bower R. G., Benson A. J., Malbon R., Helly J. C., Frenk C. S., Baugh C. M., Cole S., Lacey C. G., 2006, MNRAS, 370, 645
- Cano-Díaz M., Maiolino R., Marconi A., Netzer H., Shemmer O., Cresci G., 2012, A&A, 537, L8
- Cardamone et al. C. N., 2010, APJS, 189, 270
- Cattaneo A., Bernardi M., 2003, MNRAS, 344, 45
- Chapman S. C., Blain A. W., Smail I., Ivison R. J., 2005, ApJ, 622, 772
- Chapman S. C., Smail I., Blain A. W., Ivison R. J., 2004, ApJ, 614, 671
- Clements et al. D. L., 2008, MNRAS, 387, 247
- Colina L., Arribas S., Borne K. D., 1999, ApJL, 527, L13
- Colina L., Arribas S., Monreal-Ibero A., 2005, ApJ, 621, 725
- Coppin K., Chapin E. L., Mortier A. M. J., Scott S. E., Borys C., Dunlop J. S., Halpern M., Hughes 2006, MNRAS, 372, 1621
- Coppin et al. K., 2008, MNRAS, 389, 45
- Cowie L. L., Barger A. J., Kneib J.-P., 2002, AJ, 123, 2197
- Cox T. J., Dutta S. N., Di Matteo T., Hernquist L., Hopkins P. F., Robertson B., Springel V., 2006, ApJ, 650, 791
- Crenshaw D. M., Kraemer S. B., George I. M., 2003, ARAA, 41, 117
- Crenshaw D. M., Schmitt H. R., Kraemer S. B., Mushotzky R. F., Dunn J. P., 2010, ApJ, 708, 419
- Croton et al. D. J., 2006, MNRAS, 365, 11
- Dalla Vecchia C., Schaye J., 2008, MNRAS, 387, 1431
- Danielson A. L. R., Lehmer B. D., Alexander D. M., Brandt W. N., Luo B., Miller N., Xue Y. Q., Stott J. P., 2012, MNRAS, p. 2616
- Davies R. I., 2007, MNRAS, 375, 1099
- Debuhr J., Quataert E., Ma C.-P., 2012, MNRAS, 420, 2221
- Di Matteo T., Springel V., Hernquist L., 2005, Nature, 433, 604
- Dimitrijević M. S., Popović L. Č., Kovačević J., Dačić M., Ilić D., 2007, MNRAS, 374, 1181
- Elvis et al. M., 1994, APJS, 95, 1
- Engel et al. H., 2010, ApJ, 724, 233
- Faucher-Giguere C.-A., Quataert E., 2012, ArXiv e-prints, 1204.2547
- Feruglio C., Maiolino R., Piconcelli E., Menci N., Aussel H., Lamastra A., Fiore F., 2010, A&A, 518, L155+
- Fu H., Stockton A., 2009, ApJ, 690, 953
- Ganguly R., Brotherton M. S., 2008, ApJ, 672, 102
- Gerssen J., Wilman D. J., Christensen L., Bower R. G., Wild V., 2009, MNRAS, 393, L45
- Gibson et al. R. R., 2009, ApJ, 692, 758
- Gofford et al. J., 2011, MNRAS, 414, 3307
- Greene J. E., Ho L. C., 2005, ApJ, 627, 721
- Greene J. E., Zakamska N. L., Ho L. C., Barth A. J., 2011, ApJ, 732, 9
- Hainline L. J., Blain A. W., Smail I., Alexander D. M., Armus L., Chapman S. C., Ivison R. J., 2011, ApJ, 740, 96
- Hainline L. J., Blain A. W., Smail I., Frayer D. T., Chapman S. C., Ivison R. J., Alexander D. M., 2009, ApJ, 699, 1610
- Heckman T. M., Armus L., Miley G. K., 1990, APJS, 74, 833
- Heckman T. M., Kauffmann G., Brinchmann J., Charlot S., Tremonti C., White S. D. M., 2004, ApJ, 613, 109
- Heckman T. M., Miley G. K., van Breugel W. J. M., Butcher H. R., 1981, ApJ, 247, 403
- Helou G., Soifer B. T., Rowan-Robinson M., 1985, ApJL, 298, L7
- Hickox et al. R. C., 2012, MNRAS, 421, 284
- Holt J., Tadhunter C. N., Morganti R., 2008, MNRAS, 387, 639
- Hopkins P. F., Hernquist L., Cox T. J., Di Matteo T., Robertson B., Springel V., 2006, APJS, 163, 1
- Hopkins P. F., Hernquist L., Cox T. J., Kereš D., 2008, APJS, 175, 356
- Hopkins P. F., Hernquist L., Martini P., Cox T. J., Robertson B., Di Matteo T., Springel V., 2005, ApJL, 625, L71
- Hopkins P. F., Richards G. T., Hernquist L., 2007, ApJ, 654, 731
- Ibar E., Ivison R. J., Best P. N., Coppin K., Pope A., Smail I., Dunlop J. S., 2010, MNRAS, 401, L53
- Ivison R. J., Papadopoulos P. P., Smail I., Greve T. R., Thomson A. P., Xilouris E. M., Chapman S. C., 2011, MNRAS, 412, 1913
- Ivison R. J., Smail I., Papadopoulos P. P., Wold I., Richard J., Swinbank A. M., Kneib J.-P., Owen F. N., 2010, MNRAS, 404, 198
- Ivison et al. R. J., 2002, MNRAS, 337, 1
- Ivison et al. R. J., 2007, MNRAS, 380, 199
- Kennicutt Jr. R. C., 1998, ARAA, 36, 189
- Kewley L. J., Groves B., Kauffmann G., Heckman T., 2006, MNRAS, 372, 961
- King A., 2005, ApJL, 635, L121
- King A. R., Zubovas K., Power C., 2011, MNRAS, 415, L6
- Kovács A., Chapman S. C., Dowell C. D., Blain A. W., Ivison R. J., Smail I., Phillips T. G., 2006, ApJ, 650, 592
- Le Tiran L., Lehnert M. D., van Driel W., Nesvadba N. P. H., Di Matteo P., 2011, A&A, 534, L4
- Ledlow M. J., Smail I., Owen F. N., Keel W. C., Ivison R. J., Morrison G. E., 2002, ApJL, 577, L79
- Lehnert M. D., Nesvadba N. P. H., Le Tiran L., Di Matteo P., van Driel W., Douglas L. S., Chemin L., Bournaud F., 2009, ApJ, 699, 1660
- Leitherer C., Schaerer D., Goldader J. D., González Delgado R. M., Robert C., Kune D. F., de Mello D. F., Devost D., Heckman T. M., 1999, APJS, 123, 3
- Lutz D., Maiolino R., Spoon H. W. W., Moorwood A. F. M., 2004, A&A, 418, 465
- Maiolino et al. R., 2012, ArXiv e-prints, 1204.2904
- Matsuoka Y., 2012, ApJ, 750, 54
- McCarthy I. G., Schaye J., Bower R. G., Ponman T. J., Booth C. M., Dalla Vecchia C., Springel V., 2011, MNRAS, 412, 1965
- Menéndez-Delmestre et al. K., 2009, ApJ, 699, 667
- Menéndez-Delmestre et al. K., 2012, ApJ submitted
- Miller N. A., Fomalont E. B., Kellermann K. I., Mainieri V., Norman C., Padovani P., Rosati P., Tozzi P., 2008, APJS, 179, 114
- Morrison G. E., Owen F. N., Dickinson M., Ivison R. J., Ibar E., 2010, APJS, 188, 178
- Mullaney J. R., Alexander D. M., Goulding A. D., Hickox R. C.,

- 2011, MNRAS, 414, 1082
- Navarro J. F., Frenk C. S., White S. D. M., 1996, ApJ, 462, 563
- Nesvadba N. P. H., Lehnert M. D., De Breuck C., Gilbert A., van Breugel W., 2007, A&A, 475, 145
- Nesvadba N. P. H., Lehnert M. D., De Breuck C., Gilbert A. M., van Breugel W., 2008, A&A, 491, 407
- Nesvadba N. P. H., Lehnert M. D., Eisenhauer F., Gilbert A., Tecza M., Abuter R., 2006, ApJ, 650, 693
- Nesvadba N. P. H., Polletta M., Lehnert M. D., Bergeron J., De Breuck C., Lagache G., Omont A., 2011, MNRAS, 415, 2359
- Nesvadba et al. N. P. H., 2007, ApJ, 657, 725
- Osterbrock D. E., 1989, Astrophysics of gaseous nebulae and active galactic nuclei. University Science Books
- Page M. J., Carrera F. J., Stevens J. A., Ebrero J., Blustin A. J., 2011, MNRAS, 416, 2792
- Rafferty D. A., Brandt W. N., Alexander D. M., Xue Y. Q., Bauer F. E., Lehmer B. D., Luo B., Papovich C., 2011, ApJ, 742, 3
- Reeves J. N., O'Brien P. T., Ward M. J., 2003, ApJL, 593, L65
- Richards et al. G. T., 2006, APJS, 166, 470
- Riechers D. A., Hodge J., Walter F., Carilli C. L., Bertoldi F., 2011, ApJL, 739, L31
- Robson I., 1996, Active galactic nuclei. Wiley
- Rupke D. S., Veilleux S., Sanders D. B., 2005a, APJS, 160, 87
- Rupke D. S., Veilleux S., Sanders D. B., 2005b, APJS, 160, 115
- Rupke D. S. N., Veilleux S., 2011, ApJL, 729, L27+
- Sanders D. B., Soifer B. T., Elias J. H., Madore B. F., Matthews K., Neugebauer G., Scoville N. Z., 1988, ApJ, 325, 74
- Scott et al. S. E., 2002, MNRAS, 331, 817
- Silk J., Rees M. J., 1998, A&A, 331, L1
- Silverman et al. J. D., 2008, ApJ, 679, 118
- Simpson et al. C., 2006, MNRAS, 372, 741
- Simpson et al. C., 2012, MNRAS, 421, 3060
- Smail I., Chapman S. C., Blain A. W., Ivison R. J., 2004, ApJ, 616, 71
- Smail I., Chapman S. C., Ivison R. J., Blain A. W., Takata T., Heckman T. M., Dunlop J. S., Sekiguchi K., 2003, MNRAS, 342, 1185
- Smolčić et al. V., 2009, ApJ, 696, 24
- Springel V., Di Matteo T., Hernquist L., 2005, MNRAS, 361, 776
- Swinbank A. M., Chapman S. C., Smail I., Lindner C., Borys C., Blain A. W., Ivison R. J., Lewis G. F., 2006, MNRAS, 371, 465
- Swinbank A. M., Smail I., Chapman S. C., Blain A. W., Ivison R. J., Keel W. C., 2004, ApJ, 617, 64
- Swinbank et al. A. M., 2005, MNRAS, 359, 401
- Tacconi et al. L. J., 2008, ApJ, 680, 246
- Takata T., Sekiguchi K., Smail I., Chapman S. C., Geach J. E., Swinbank A. M., Blain A., Ivison R. J., 2006, ApJ, 651, 713
- Tamura Y., Kohno K., Nakanishi K., Hatsukade B., Iono D., Wilson G. W., Yun M. S., Takata T., 2009, Nature, 459, 61
- Tombesi F., Cappi M., Reeves J. N., Braitto V., 2012, MNRAS, 422, L1
- Trump et al. J. R., 2006, APJS, 165, 1
- Valiante E., Lutz D., Sturm E., Genzel R., Tacconi L. J., Lehnert M. D., Baker A. J., 2007, ApJ, 660, 1060
- van de Voort F., Schaye J., Booth C. M., Dalla Vecchia C., 2011, MNRAS, 415, 2782
- Veilleux S., Cecil G., Bland-Hawthorn J., 2005, ARAA, 43, 769
- Veilleux S., Kim D.-C., Sanders D. B., 1999, ApJ, 522, 113
- Villar-Martín M., Humphrey A., Delgado R. G., Colina L., Arribas S., 2011, MNRAS, 418, 2032
- Villar-Martín M., Tadhunter C., Humphrey A., Encina R. F., Delgado R. G., Torres M. P., Martínez-Sansigre A., 2011, MNRAS, 416, 262
- Wardlow et al. J. L., 2011, MNRAS, 415, 1479
- Webb et al. T. M., 2003, ApJ, 587, 41
- Westmoquette M., Clements D., Bendo G., Khan S., 2012, ArXiv e-prints, 1205.0203
- Willott C. J., Rawlings S., Blundell K. M., Lacy M., 1998, MNRAS, 300, 625
- Zheng X. Z., Xia X. Y., Mao S., Wu H., Deng Z. G., 2002, AJ, 124, 18
- Zubovas K., King A., 2012, ApJL, 745, L34

APPENDIX A: NOTES ON INDIVIDUAL SOURCES

Here we provide background notes on each source from our sample and provide some more details of our analysis on individual sources that is not required for the overall discussion given in the main text. The 1.4 GHz flux densities are provided in Table 1 and the infrared and sub-mm flux densities are provided in Table 2. All of the parameters for the profile fits to the galaxy-integrated spectra (see Fig. 3) and spectra extracted from different regions (see Fig. 5) are provided in Table 3 and Table 4 respectively.

A1 SMM J0217-0503

This source was first identified as a sub-mm and radio source by Coppin et al. (2006) and Simpson et al. (2006) respectively. IFU emission around the H α emission line reveal at least two merging components (Alaghband-Zadeh et al. 2012) over ≈ 20 –25 kpc. Our IFU observations of the [O III] emission line also reveal at least two systems separated by $\approx 3''$ (≈ 25 kpc; see Fig. 4). The northern system has broad H α emission in the central regions (FWHM ≈ 940 km s $^{-1}$; Alaghband-Zadeh et al. priv. comm.) and a high [N III]/H α ≈ 1.1 –1.3 ratio (Alaghband-Zadeh priv. comm). Along with our measured ratio [O III]/H β > 1.3 this suggests that this source is most likely hosting AGN activity (e.g. Kewley et al. 2006). In Fig. 5 we show that the [O III] kinematics in this northern component also displays the signatures of an outflow; i.e. a broad emission line (FWHM = 900 ± 400 km s $^{-1}$) which has a high velocity offset from the H α emission ($\Delta v = -460 \pm 60$ km s $^{-1}$; Fig. 6). Due to the complexity of blending between the [N II] doublet and H α line, it is not possible to confirm if this outflowing component is also present in the H α emission-line profile. The broad [O III] emission in this northern component is spatially unresolved (≤ 4.0 kpc) and has a modest signal-to-noise ratio such that we do not have strong evidence for a galaxy-wide outflow in this source.

The southern system has H α emission extended over ≈ 10 kpc with kinematics which may be described by a rotating disk; however, the double peaked emission line and a large gradient in the [N II]/H α ratio from east to west could also indicate that this southern system has undergone a recent merger (Alaghband-Zadeh et al. 2012). Our observations of the [O III] emission line displays a redshift, line-width and position that is only consistent with the western ≈ 5 kpc of the H α emission, with no [O III] detected in the eastern side. The [O III] emission is located where the [N II]/H α ratio is lowest suggesting a different chemical composition across the galaxy, as opposed to excitation effects (e.g., Kewley et al. 2006). These observations are consistent with the scenario that this southern system may have undergone a recent merger.

A2 SMM J0302+0006

This sub-mm source was first detected by Webb et al. (2003). Optical and near-IR spectra show a high $[\text{N II}]/\text{H}\alpha = 1.38 \pm 0.07$ line ratio, and *Spitzer* mid-infrared spectroscopic observations show an excess in the mid-infrared continuum suggesting AGN activity (Swinbank et al. 2004; Chapman et al. 2005; Menéndez-Delmestre et al. 2009). *HST* imaging and $\text{H}\alpha$ IFU data show this source contains two components separated by ≈ 11 kpc (Swinbank et al. 2006; Menéndez-Delmestre et al. 2012).

The galaxy-integrated $[\text{O III}]$ emission we observe is broad ($\text{FWHM} = 900 \pm 300 \text{ km s}^{-1}$; Fig. 3) but is spatially unresolved (≤ 3.6 kpc). However, due to the low signal-to-noise ratio of the integrated spectrum we cannot rule out the existence of low surface brightness extended emission. No $\text{H}\beta$ emission was detected in the galaxy-integrated spectrum, with a 3σ upper limit on the flux of $F_{\text{H}\beta} < 8 \times 10^{-17} \text{ erg s}^{-1} \text{ cm}^{-2}$ (assuming the line-width is the same as that measured for $[\text{O III}]$).

A3 RG J0302+0010

This source was first identified by Chapman et al. (2004). This source has rest-frame UV spectroscopy that reveals strong $[\text{C IV}]$ emission, which along with the high $[\text{N II}]/\text{H}\alpha = 1.13 \pm 0.4$ line ratio implies AGN activity (Chapman et al. 2004; Swinbank et al. 2004). Observations with long-slit spectroscopy show that the $[\text{O III}]$ emission is broad and has an asymmetric line profile (Takata et al. 2006).

The galaxy-integrated spectrum around the $[\text{O III}]\lambda\lambda 4959, 5007$ emission-line doublet reveals both a narrow and redshifted broad component (Fig. 3). The broad component is located in the central ≈ 8 kpc, where the line ratio $[\text{O III}]/\text{H}\beta = 9 \pm 3$ implies bright AGN activity (Fig. 5). We confirmed the broad emission line was spatially extended by integrating spectra in two $0.6'' \times 0.6''$ bins, one in the north of the emission-line region and one in the south. We fit these spectra following the methods outlined in §3 and found that the broad emission line has a velocity shear of $125 \pm 30 \text{ km s}^{-1}$ which is broadly consistent with the velocity gradient observed in Fig. 6.

The broad $[\text{O III}]$ emission line is most likely due to an outflow with the near-side of the outflow being obscured by dust (see §5.2 for a full discussion). Blueshifted broad components are more commonly associated with outflows (e.g., Heckman et al. 1981) as opposed to the redshifted broad component we observe here. However, redshifted broad components are observed in a fraction of local AGN and can be explained by the relative orientations of the AGN and obscuring material in host galaxy (e.g., Barth et al. 2008; Crenshaw et al. 2010). In particular IFU observations of the local interacting Seyfert galaxy LEDA 135736, identify a broad, redshifted outflow associated with AGN activity, which could be a low redshift analogue of this source (Gerssen et al. 2009).

A4 RG J0332-2732

IFU observations of this source reveals that $\text{H}\alpha$ is extended over ≈ 10 kpc with velocity offsets of $\Delta v \lesssim 200 \text{ km s}^{-1}$ across the galaxy. The brightest region (Fig. 5; Table 4) has a high $[\text{O III}]/\text{H}\beta > 4.0$ line ratio, which along with the high $[\text{N II}]/\text{H}\alpha = 0.8 \pm 0.1$ line ratio (Alaghband-Zadeh et al. 2012) suggests AGN activity (e.g., Kewley et al. 2006).

The $[\text{O III}]$ emission-line kinematics (Fig. 4; Fig. 6)

appear to be tracing similar kinematics to the $\text{H}\alpha$ emission line (Alaghband-Zadeh et al. 2012) with similar line widths ($\text{FWHM} \approx 200\text{--}700 \text{ km s}^{-1}$) and velocity gradients ($\Delta v \lesssim 200 \text{ km s}^{-1}$). The $[\text{O III}]$ emission is more extended to the north than the $\text{H}\alpha$ emission and, along with the observation that the $[\text{N II}]/\text{H}\alpha$ ratio is highest in the north (Alaghband-Zadeh et al. 2012), suggests the presence of an AGN ionisation cone.

Unlike the majority of our sample with spatially resolved data, we are unable to fit multiple components to the emission line profile and are unable to de-couple the signatures of an outflow from the galaxy dynamics. However, we note that the emission lines in the brightest regions display very large widths (FWHM up to $\approx 700 \text{ km s}^{-1}$; Fig. 6), which are broader than the narrow lines we associate with galaxy dynamics in the other sources ($\approx 100\text{--}500 \text{ km s}^{-1}$; Fig. 7). Although not as well defined as in the other sources, we speculate that an outflow could be responsible for these large line widths.

A5 SMM J0943+4700

This sub-mm source was first identified by Cowie et al. (2002) and is modestly lensed (amplification of 1.2). Ledlow et al. (2002) identified two radio counterparts separated by ≈ 30 kpc in projection and labelled them as H6 and H7. The latter shows narrower and fainter $[\text{O III}]$ emission than its companion but dominates the sub-mm and CO emission, indicating that the bulk of star formation is occurring in this component (Takata et al. 2006; Valiante et al. 2007; Engel et al. 2010; Riechers et al. 2011). An excess in the mid-infrared continuum observed in *Spitzer* mid-infrared spectroscopy indicate the presence of AGN activity in this source (Valiante et al. 2007) although both H6 and H7 are covered by this spectra. H6, the source observed in our observations, has rest-frame UV emission-line widths, and line ratios indicative of a narrow-line Seyfert 1 galaxy (Ledlow et al. 2002). Additionally long-slit near-IR spectroscopy of H6 reveals $[\text{O III}]$ emission that is broad and extended over $\approx 3''\text{--}4''$ (Takata et al. 2006), indicative of an outflow.

Using our IFU observations we find that the $[\text{O III}]$ emission from this source is very extended (≈ 20 kpc) with a complex morphology and kinematic structure (Fig. 4). The north-western region shows modest $[\text{O III}]$ line-widths ($\text{FWHM} = 200\text{--}300 \text{ km s}^{-1}$) consistent with being due to galaxy dynamics and merger remnants (Fig. 7; see § 5.1 for a discussion). In addition there is extremely broad $[\text{O III}]$ emission ($\text{FWHM} = 1000\text{--}1400 \text{ km s}^{-1}$) extended over ≈ 15 kpc (Fig. 5 and Fig. 6), which we attribute to an energetic outflow. Despite observing modest velocity offsets between the narrow and broad $[\text{O III}]$ emission lines ($\Delta v \leq 150 \text{ km s}^{-1}$; Fig. 6), there is clearly extremely turbulent ionised gas over a considerable extent. The zero velocity offset between the broad and narrow $[\text{O III}]$ components in the spatially-integrated spectra (Fig. 3 and Fig. 5) could be explained if we are observing an outflow orientated in the plane of the sky.

A6 SMM J1235+6215

This source was identified as a sub-mm bright galaxy by Chapman et al. (2005). Deep *Chandra* images shows that it hosts a heavily obscured X-ray luminous AGN ($L_{0.5\text{--}8\text{keV}} = 10^{44.0} \text{ erg s}^{-1}$; $N_{\text{H}} = 10^{24} \text{ cm}^{-2}$; Alexander et al. 2005). An excess in the mid-infrared continuum observed in *Spitzer* mid-infrared spectroscopy further suggests the presence of AGN activity in this source

(Menéndez-Delmestre et al. 2009). IFU observations reveal a bright compact (≈ 3 kpc) source of broad H α emission (FWHM $\gtrsim 1000$ km s $^{-1}$) attributed to AGN activity and spatially offset ($\approx 0.5''$) from the narrower H α emission (FWHM ≈ 500 – 800 km s $^{-1}$), which is likely to be dominated by star-formation activity (Menéndez-Delmestre et al. 2012). Long-slit near-IR spectroscopy suggest that the [O III] emission is extended over $\approx 1''$ (≈ 8 kpc; Takata et al. 2006).

The galaxy-integrated spectrum around the [O III] $\lambda\lambda 4959, 5007$ emission-line doublet reveals an extremely broad emission line (FWHM = 1500 ± 500 km s $^{-1}$) which may suggest an outflow (Fig. 3). Takata et al. (2006) find that this source has extended [O III] emission over $\approx 1''$. Although we find tentative evidence that the [O III] emission is marginally extended ($\approx 0.8''$; 7 kpc) in our data we are unable to constrain the properties of the extended emission due to insufficient signal-to-noise ratio of the data to fit the emission-line profiles.

We also detect H β emission, at a redshift of $z_{\text{H}\beta} = 2.2031 \pm 0.0006$, with a width of $\text{FWHM}_{\text{H}\beta} = 500 \pm 200$ km s $^{-1}$ and flux $F_{\text{H}\beta} = 0.9 \pm 0.2 \times 10^{-16}$ erg s $^{-1}$ cm $^{-2}$, extended over $\approx 1''$ (≈ 8 kpc). The extremely broad [O III] emission we observe is offset from the H β emission $\Delta v \approx -400 \pm 200$ km s $^{-1}$. Although there is weak evidence for an extended outflow in this source, deeper observations are required to confirm this.

A7 SMM J1237+6203

This source was identified as a sub-mm bright galaxy by Chapman et al. (2005). The bright optical counterpart ($R = 20.2$; Chapman et al. 2005), X-ray luminosity ($L_{0.5-8\text{keV}} = 10^{44.3}$ erg s $^{-1}$; Alexander et al. 2005) and optical-near-IR spectroscopy that reveal broad emission lines (Ly α ; N V; C IV; H γ -H α ; FWHM ≈ 2100 - 2700 km s $^{-1}$; Chapman et al. 2005; Takata et al. 2006; Coppin et al. 2008), result in this source being classified as a broad-line quasar, with a virial BH mass of $\log(M_{\text{BH}}) = 8.2 M_{\odot}$ (Alexander et al. 2008).

IFU observations around redshifted [O III] of SMM J1237+6203 were first presented in Alexander et al. (2010) where a complete discussion of the source is provided. We note the orientation of this source in Alexander et al. (2010) is flipped in the east-west direction and the correct orientation is given in this work (Fig. 4). In addition we provide updated [O III] flux and luminosity measurements.

The galaxy-integrated spectrum around the [O III] emission line (Fig. 3) shows a bright narrow component with a prominent blue-wing. This type of profile is most commonly interpreted as being the result of an AGN-driven outflow (e.g., Heckman et al. 1981; Nesvadba et al. 2008). The velocity and FWHM profiles (Fig. 6) show that the narrow emission has a small velocity gradient of $\Delta v \approx 200$ km s $^{-1}$ across the galaxy and is likely to be tracing the host galaxy dynamics (also see Alexander et al. 2010). In contrast, the broad [O III] component (FWHM ≈ 1000 km s $^{-1}$) is offset from the narrow component by ≈ -350 km s $^{-1}$, over ≈ 5 kpc, providing strong evidence for an outflow in this region. Although the broad component is only formally fit over ≈ 5 kpc, low surface brightness broad emission exists up to ≈ 8 kpc in total extent (Alexander et al. 2010).

We also identify H β emission in the galaxy-integrated spectrum, with a redshift of $z = 2.0754[2]$ and flux $F_{\text{H}\beta} = 1.1 \pm 0.4 \times 10^{-15}$ erg s $^{-1}$ cm $^{-2}$. The width of the H β emission line (FWHM = 2030 ± 70 km s $^{-1}$) indicates the presence

of a broad-line region, which is consistent with that found from H α observations of this source (Coppin et al. 2008).

A8 SMM J1636+4057

This sub-mm source was first identified by Scott et al. (2002) and Ivison et al. (2002). *Hubble Space Telescope* (HST) ACS and NICMOS observations reveal a complex galactic morphology with at least three merging or interacting components, covering ≈ 8 – 15 kpc in projection (Swinbank et al. 2005; see Fig. A1). An excess in the mid-infrared continuum observed in the *Spitzer* mid-infrared spectroscopy indicate the presence of AGN activity in this source (Menéndez-Delmestre et al. 2009). Long-slit and IFU near-IR spectroscopy reveal a broad-line AGN (broad spatially unresolved H α and H β emission with FWHM ≈ 2000 – 3000 km s $^{-1}$) and narrow H α emission traces star-formation along the UV bright arc shown in the HST image (Fig. A1; Smail et al. 2003; Swinbank et al. 2005; Menéndez-Delmestre et al. 2012). The broad-line AGN is found at $\Delta v \approx 700$ km s $^{-1}$ from the narrow H α emission, providing further evidence that this system is undergoing a merger. The presence of a molecular gas cloud in the southern regions of the system is shown through high and low excitation CO emission-line gas (Tacconi et al. 2008; Engel et al. 2010; Ivison et al. 2011). Previous long-slit observations show that the [O III] emission is kinematically complex and spatially extended (≈ 1 – $2''$) with broad components (FWHM $\lesssim 2000$ km s $^{-1}$; Smail et al. 2003; Takata et al. 2006), providing initial evidence for an energetic outflow.

Our galaxy-integrated spectrum around the [O III] $\lambda\lambda 4959, 5007$ emission-line doublet (Fig. 3) reveals a prominent narrow component and two broad components separated by $\Delta v = 1700 \pm 100$ km s $^{-1}$. We are confident that the broad redshifted emission line is also from [O III] as Smail et al. (2003) also identify [Ne V] and N V emission lines at approximately this redshift.

In Fig. 4 we show that the [O III] emission-line morphology, velocity field and FWHM map from our IFU observations. Narrow [O III] emission ($100 \lesssim \text{FWHM} \lesssim 500$ km s $^{-1}$) is extended over $\approx 1''$ (≈ 8 kpc) to the north of the peak in surface brightness, associated with faint infrared emission in the HST image, and fainter narrow emission is observed $\approx 1''$ to the south; this is consistent with the long-slit observations of Smail et al. (2003) (also see Fig. A1). The redshift of this narrow [O III] emission is consistent with the molecular gas and H α arc and therefore is likely to be tracing merger remnants and galaxy dynamics (e.g., Fig. 6). We also detect faint H β emission that is spatially coincident with the star-forming arc (Fig. A1).

The two broad [O III] emission-line components (FWHM ≈ 1200 km s $^{-1}$) are spatially coincident with the broad H α emission line (Fig. 5 and Fig. A1) and are moderately spatially extended ($\approx 0.8''$; ≈ 7 kpc). We verified that the broad emission lines were intrinsically spatially extended by extracting spectra from two $0.6'' \times 0.6''$ bins; one in the north and one in the south of the observed broad [O III] region. We found that that the ratio of the two broad components changed from north to south. The redshifted broad component dominates in the north and the blueshifted broad component dominates in the south, which is also demonstrated in the velocity map of this source (Fig. 4). The broad [O III] components are offset from the broad H α emission line by $\Delta v \approx \pm 850$ km s $^{-1}$ (Fig. 6; Swinbank et al. 2005), indicating that we are observing both sides of an outflow (e.g., Nesvadba et al. 2008). To verify that the broad H α is due to a true broad-line

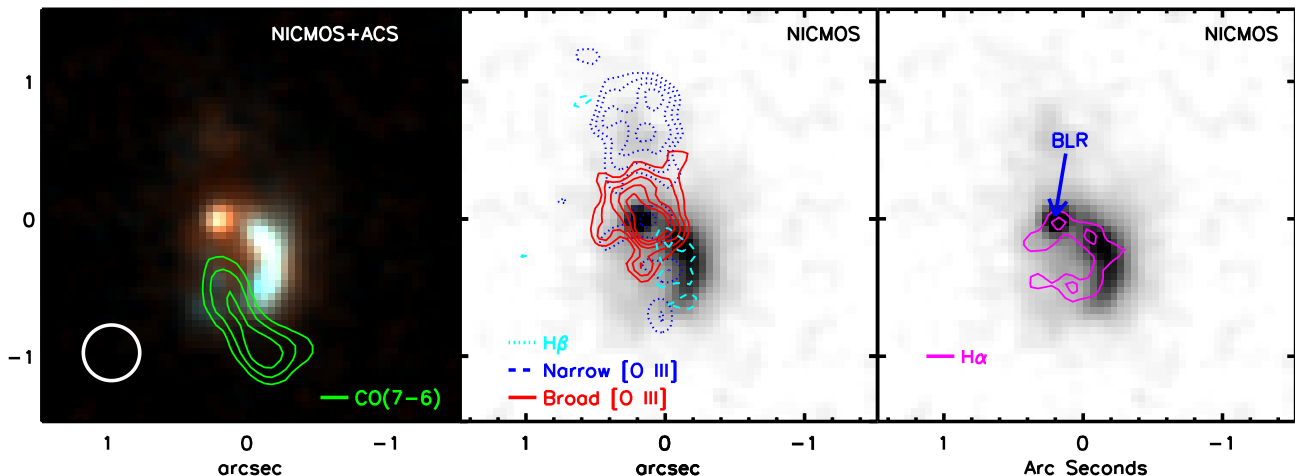


Figure A1. *Left:* True colour $I_{814}H_{160}$ image of SMM J1636+4057 from the *HST* ACS and NICMOS imaging (Swinbank et al. 2005). The contours denote the intensity of the velocity integrated CO(7–6) millimetre emission (Tacconi et al. 2008). The circle denotes the approximate seeing disk of our observations. *Middle:* *HST* NICMOS H_{160} grey-scale image with contours overlaid of narrow band (wavelength collapsed) images from our IFU observations. The solid contours denote the extent/intensity of the broad [O III] emission, which is associated with the red continuum seen in the colour image. The dotted contours denote the extent/intensity of the narrow [O III] for which the majority is associated with faint emission observed to the north of the red continuum peak. The dashed contours denote the H β emission which is spatially coincident with the blue arc in the *HST* image. *Right:* The same image as in the central panel but with the contours from the IFU+adaptive optics H α observations of Menéndez-Delmestre et al. (2012) overlaid. There is extremely broad (FWHM \approx 2700 km s $^{-1}$) unresolved H α emission, attributed to an AGN broad line region (BLR) and narrower spatially extended emission along the blue arc, which is attributed to star formation. The field-of-view of these H α observations did not cover the region of narrow [O III] emission seen in the north of the middle panel. North is up and east is left.

region, as opposed to dynamics in the host galaxy, we attempted to re-fit the spectrum of Swinbank et al. (2005) with a narrow-line Gaussian component plus two additional Gaussian components with the same redshifts and line-widths of the broad [O III] emission lines (e.g., similar to the methods used by Cano-Díaz et al. 2012 and Mullaney et al. in prep). We found that this did not adequately describe the H α emission-line profile and an additional broad component is still required (with FWHM \approx 2700 km s $^{-1}$ and $z = 2.393 \pm 0.005$; consistent with Swinbank et al. 2005) providing strong evidence of a true AGN broad-line region.

The outflow we observe is spatially coincident with the AGN in this source, and no outflow is observed in the region of unobscured star-formation (the UV bright arc). We conclude that the broad [O III] emission lines we see are due a bi-polar AGN-driven outflow at $v \approx \pm 850$ km s $^{-1}$.

A9 SMM J2217+0010

This source was first identified by Smail et al. (2004) and Chapman et al. (2005). An excess in the mid-infrared continuum observed in the *Spitzer* mid-infrared spectroscopy suggests the presence of AGN activity in this source (Menéndez-Delmestre et al. 2009). The results of Takata et al. (2006) suggest bright [O III] emission ($F_{[\text{OIII}]} = 6.0 \times 10^{-16}$ erg s $^{-1}$ cm $^{-2}$) and a high [O III]/H $\beta \approx 10$ ratio further indicating AGN activity. However in our observations [O III] $\lambda\lambda$ 4959,5007 emission was undetected. By spatially integrating over the extent of a seeing disk and assuming an emission line with a FWHM of 500 km s $^{-1}$, we infer a 3σ upper limit on the [O III] flux (luminosity) of $F_{[\text{OIII}]} < 4.6 \times 10^{-17}$ erg s $^{-1}$ cm $^{-2}$ ($L_{[\text{OIII}]} < 2.6 \times 10^{42}$ erg s $^{-1}$). This upper limit is considerably lower than the value quoted in Takata et al. (2006) which may arise

due to the presence a strong sky-line at the observed wavelength of the [O III] λ 5007 emission line in this source, potentially resulting in an excess measurement of the flux quoted in Takata et al. (2006).

A10 SMM J2217+0017

This source was identified as a sub-mm bright galaxy by Tamura et al. (2009). We did not detect [O III] $\lambda\lambda$ 4959,5007 emission. This source was detected in H α emission in the same data cube (Alaghband-Zadeh et al. 2012), therefore the non-detection is due to an [O III] flux that is below our detection threshold. Assuming an emission line of a FWHM of 350 km s $^{-1}$ (to match the H α observations; Alaghband-Zadeh et al. 2012) and integrating over the spatial extent of the H α emission, we infer a 3σ upper limit on the [O III] flux (luminosity) of $F_{[\text{OIII}]} < 2.6 \times 10^{-17}$ erg s $^{-1}$ cm $^{-2}$ ($L_{[\text{OIII}]} < 1.0 \times 10^{42}$ erg s $^{-1}$).